Skillful Seasonal Tropical Cyclone Prediction with AI Weather–Climate Models Forced by Dynamically Predicted SSTs

Hiroyuki Murakami[a] and Baoqiang Xiang[a,b]

[a] *National Oceanic and Atmospheric Administration/Geophysical Fluid Dynamics Laboratory, Princeton, New Jersey, USA*

[b] *University Corporation for Atmospheric Research, Boulder, CO, USA*

Submitted to the *Journal of Climate* on September 21, 2026

Corresponding author: Hiroyuki Murakami, NOAA/GFDL, 201 Forrestal Rd., Princeton, NJ 08540-6649. E-mail: hir.murakami@gmail.com

ABSTRACT: AI weather–climate models are far cheaper than dynamical seasonal prediction models and have shown skillful tropical cyclone (TC) prediction under persisted sea surface temperature (SST) anomalies, but their skill under dynamically predicted ocean boundary conditions, benchmarked against an established dynamical seasonal prediction system, is untested. We evaluate eight seasonal hindcast configurations against GFDL-SPEAR, the coupled model behind GFDL's real-time forecasts, over 1993–2025 for the July–November season in the western North Pacific, eastern North Pacific, and North Atlantic. The hybrid NeuralGCM and data-driven ACE2 use predicted SST and sea ice from operational models; six NeuralGCM configurations differ only in their SST source. Their advantage over SPEAR is basin-, metric-, and lead-dependent. At zero-month lead, six of seven AI-based configurations achieve North Atlantic correlations of 0.60–0.76, versus SPEAR's 0.59. At the grid-point scale, nearly every AI-based configuration exceeds SPEAR's significant-skill area in the eastern North Pacific and North Atlantic by up to 20–25 percentage points, and one retains skill at four-month lead where SPEAR does not; SPEAR remains unmatched for accumulated cyclone energy in the western North Pacific. TC prediction skill reflects a complex interplay among biases in a configuration's TC climatology, large-scale environment, and genesis response to it, so higher skill can arise from compensating biases rather than a physically valid mechanism. Overall, the rapid advancement of AI weather–climate models, together with the enduring value of dynamical models, suggests considerable potential for hybrid dynamical–AI approaches to advance seasonal TC prediction.

SIGNIFICANCE STATEMENT: Months in advance, forecasters try to predict whether the coming season will bring many hurricanes and typhoons or only a few. These outlooks normally rely on large, physics-based computer models that are costly to run. We tested whether new artificial-intelligence models can provide similar predictions when supplied with forecasts of how ocean temperatures will evolve. Our results show that they can: over the Atlantic and eastern Pacific, they matched or outperformed a leading physics-based model at a small fraction of the computational cost, and one remained useful at longer lead times. However, they did not perform better everywhere, and a model can sometimes produce the right answer for the wrong physical reason. Used alongside conventional forecasts, these tools could make seasonal storm prediction more computationally efficient and potentially more skillful.

1. Introduction

Tropical cyclones (TCs) are among the most devastating and costliest natural hazards worldwide, causing substantial loss of life and economic damage each year (Krichene et al. 2023; Siddik and Islam 2024). Accordingly, skillful prediction of their activity months in advance carries considerable scientific and socioeconomic value (Lemoine and Kapnick 2024). Efforts to predict seasonal TC activity date back to the early 1980s and have produced a large body of literature. Several studies have reviewed the development of seasonal TC prediction (Camargo et al. 2007; Chu and Murakami 2022; Takaya et al. 2023; Murakami and Chu 2025). Seasonal TC prediction methods fall into three broad categories: dynamical, in which TCs are objectively detected from a physics-based model's own forecast fields (e.g., Vitart and Stockdale 2001; Murakami et al. 2016b); statistical, based on empirical regression against observed large-scale predictors without a dynamical forecast (e.g., Chu and Zhao 2007; Zhang et al. 2017b); and statistical–dynamical, in which such empirical relationships are applied to a dynamical model's predicted large-scale environment (e.g., Vecchi et al. 2011; Murakami et al. 2016a; Zhang et al. 2017a). Dynamical and statistical–dynamical approaches generally outperform purely statistical ones, with statistical–dynamical methods further improving on dynamical predictions alone (Murakami and Chu 2025).

Regarding dynamical predictions, the National Oceanic and Atmospheric Administration (NOAA) Geophysical Fluid Dynamics Laboratory (GFDL) conducts semi-operational real-time seasonal dynamical forecasts for research purposes. These real-time TC predictions from GFDL are shared with the experts at the NOAA Climate Prediction Center and the National Hurricane Center, supporting their seasonal hurricane outlook, issued each May and updated in August (Takaya et al. 2023). GFDL utilizes two dynamical models for hurricane seasonal forecasts: Seamless System for Prediction and Earth System Research (SPEAR, Delworth et al. 2020; Lu et al. 2020) and a high-resolution version of the Forecast-oriented Low Ocean Resolution (FLOR) GFDL coupled model (HiFLOR, Murakami et al. 2015, 2016b; Zhang et al. 2016). Detailed forecast skill of these models is documented in Murakami et al. (2016b, 2025). One of the issues in SPEAR predictions is that prediction skill in TC activity in the North Atlantic deteriorated compared with the previous prediction model at GFDL (i.e., FLOR, Vecchi et al. 2014). Murakami et al. (2025) found that SPEAR achieves higher prediction skill for large-scale variables such as sea surface temperature (SST), wind shear, and low-level vorticity over the main TC development regions compared with FLOR, seemingly implying improved TC prediction skill as well; however, this was not the case. Murakami et al. (2025) emphasized that in order to improve TC predictions, it is not sufficient to improve large-scale environmental predictions alone; rather, improving the model's response of TCs to specific large-scale environmental conditions is important. In other words, a model that simulates a more accurate TC response to given large-scale environmental conditions than SPEAR could achieve better seasonal TC prediction skill than SPEAR, provided it is initialized with, or forced by, SPEAR's predicted large-scale environmental conditions.

Recently, new types of statistical and statistical–dynamical approaches incorporating machine learning (ML) and deep learning (DL) techniques have received much attention (e.g., Fu et al. 2023; Comaniciu and Murakami 2026). These data-driven or hybrid dynamical models utilize large datasets and advanced algorithms to capture complex patterns in TC behavior, potentially offering improved predictive skill over traditional methods (Comaniciu and Murakami 2026). Although these approaches have shown promise in various meteorological applications, applying them to seasonal TC forecasting remains challenging due to the limited availability of long-term, high-quality observational data, the rarity of TC occurrence, and the inherent complexity of TC dynamics. Therefore, model overfitting is a persistent concern in these data-driven approaches to seasonal TC prediction (Comaniciu and Murakami 2026). Another issue in the data-driven approach is the lack of physical interpretability. While these models can identify patterns and correlations in the data, they often do not provide insights into the underlying physical processes driving TC formation and evolution (e.g., Murakami et al. 2016a). This limitation can hinder the development of robust and reliable seasonal TC forecasts, as understanding the physical mechanisms is crucial for improving model performance and generalizability.

Recent advances in AI-based global atmospheric modeling have led to a new generation of models spanning applications from weather forecasting toward climate simulation, including models such as GraphCast and Pangu-Weather that were developed for medium-range weather prediction (e.g., Bi et al. 2023; Lam et al. 2023). These models are pre-trained on massive atmospheric datasets and can emulate the evolution of three-dimensional atmospheric states with substantially lower computational cost than conventional dynamical models. Their pre-trained representations can be adapted to downstream applications through transfer learning, potentially reducing overfitting when only limited datasets are available. Unlike conventional statistical or statistical–dynamical approaches that rely on manually selected predictors, AI weather–climate models learn hierarchical feature representations directly from high-dimensional atmospheric fields, reducing the dependence on subjective predictor selection and potentially capturing more complex relationships relevant to TC activity. Here, "AI weather–climate models" are broadly defined to include AI-based global atmospheric models capable of simulations across weather-to-climate timescales (Henn et al. 2026).

Recent developments have broadened the scope of AI weather–climate modeling for seasonal-to-decadal prediction. NeuralGCM (Kochkov et al. 2024), a hybrid machine learning–physics atmospheric model developed by Google, combines machine-learning parameterizations with an explicit dynamical core, providing a framework that integrates data-driven learning with numerical representations of atmospheric dynamics while maintaining dynamical consistency. In contrast, ACE2 (Watt-Meyer et al. 2025) is a deep-learning-based AI weather–climate model pre-trained on the fifth-generation ECMWF atmospheric reanalysis (ERA5; Hersbach et al. 2020) and optimized for seasonal-to-decadal simulation and prediction. Although ACE2 does not explicitly solve the governing equations of atmospheric motion, it is capable of performing stable long-term simulations while efficiently emulating the large-scale evolution of the atmosphere, making it well suited for seasonal forecasting applications (Kent et al. 2025). Despite their different architectures, both models illustrate the growing diversity of AI weather–climate models and demonstrate promising pathways toward improving seasonal-to-decadal TC prediction.

Zhang et al. (2025) pioneered the application of NeuralGCM to seasonal prediction of TC activity. Their hindcast experiments, initialized on 1 July and targeting the July–November TC season, employed a persistent-anomaly approach in which SST and sea ice follow their climatological seasonal cycle while retaining the anomalies present at initialization. This configuration yielded promising prediction skill, particularly in the North Atlantic basin where the correlation between predicted and observed TC frequency reached approximately 0.7 over 1990–2023—comparable to established dynamical predictions (Murakami and Chu 2025). Despite this encouraging performance, prediction skill was notably limited in the North Indian Ocean and the Northwest Pacific, suggesting that the model struggles to capture the full range of TC variability across basins.

A fundamental limitation of the persistent-anomaly framework is its assumption that SST anomalies observed at initialization remain fixed throughout the forecast period. While this approximation may be defensible for July initializations—when El Niño–Southern Oscillation (ENSO)-related SST variability tends to be relatively stable through boreal autumn—it becomes increasingly problematic at longer lead times (e.g., January–April initializations). At such leads, the well-known ENSO spring predictability barrier (Duan and Wei 2013) means that SST anomalies in the tropical Pacific can evolve substantially and unpredictably from their initial state, and artificially persisting those anomalies may degrade forecast skill.

To address this limitation, the present study replaces the persistent-anomaly SST and sea-ice concentration fields with fields dynamically predicted by the GFDL-SPEAR seasonal prediction model, prescribed as boundary conditions for NeuralGCM and ACE2, thereby providing a more physically consistent representation of evolving ocean states and potentially extending skillful TC predictions to longer lead times. We also use the predicted SST fields from other forecast agencies to evaluate the sensitivity of seasonal TC prediction skill to the choice of SST forcing. The primary objective of this study is to benchmark the seasonal prediction skill of ACE2 and NeuralGCM against the established dynamical models SPEAR and HiFLOR-S, focusing on basin-specific TC metrics and lead times. Beyond basin-total skill, we further ask whether differences in TC prediction skill reflect a physically valid representation of the large-scale genesis environment—its climatology, interannual variability, and the fidelity of the modeled TC-genesis response to it. This follows Murakami et al. (2025)'s finding that skill in the large-scale environment does not by itself guarantee skillful TC-activity prediction. By systematically comparing these configurations, we aim to identify strengths and weaknesses in their predictive capabilities, thereby informing future improvements in seasonal TC forecasting.

Section 2 describes the models, experimental design, skill metrics, TC detection criteria, and verification datasets. Section 3 compares climatological TC characteristics, basin-total skill by initialization month and lead time, sub-basin spatial skill, and skill in the large-scale environment and its relationship to TC genesis. Section 4 summarizes the key findings, discusses limitations, and outlines implications for operational seasonal TC forecasting.

2. Methods

a. Models

SPEAR

SPEAR (Delworth et al. 2020) is a coupled climate model developed at GFDL that combines the Atmosphere Model 4 (AM4) and Land Model 4 (LM4) (Zhao et al. 2018) with the Modular Ocean Model version 6 (MOM6) and the Sea Ice Simulator version 2 (SIS2) (Adcroft et al. 2019). The atmospheric and land components are configured at approximately 50-km horizontal resolution, while the ocean and sea ice components operate at 100-km resolution.

HiFLOR-S

HiFLOR-S is based on HiFLOR (Murakami et al. 2015, 2016b), which employs a 25-km mesh for the atmospheric and land components—finer than the 50-km resolution used in FLOR and SPEAR—while retaining the same 100-km ocean and sea ice components derived from CM2.1 (Delworth et al. 2006). In HiFLOR-S, the model's own simulated SST is nudged toward the SPEAR-predicted SST with a relaxation timescale of 5 days, allowing the high-resolution atmospheric model to respond to dynamically evolving ocean boundary conditions from the SPEAR prediction model (Murakami et al. 2025).

NeuralGCM

NeuralGCM (Kochkov et al. 2024) is a hybrid atmospheric model developed by Google that integrates a differentiable dynamical core with neural network-based parameterizations of subgrid-scale physical processes. The dynamical core solves the hydrostatic primitive equations governing large-scale atmospheric motion, while the machine-learning component handles unresolved column processes such as cloud formation, radiation, and precipitation. Earlier hybrid ML–physics models trained the ML parameterization offline, independently of the dynamical core to which it was later coupled (e.g., Brenowitz and Bretherton 2019; Yuval et al. 2021; Watt-Meyer et al. 2024). A key innovation of NeuralGCM is end-to-end training instead: the neural network is optimized jointly with the dynamical core through multi-day forecast rollouts on ERA5 reanalysis data (Hersbach et al. 2020), which promotes long-term stability. The model is available at 2.8°, 1.4°, and 0.7° horizontal resolutions, each with deterministic and stochastic variants. When driven by prescribed SST and sea-ice-boundary conditions, NeuralGCM can sustain stable multi-year climate integrations and has demonstrated the ability to generate realistic TC climatology at 1.4° resolution at a fraction of the computational cost of conventional GCMs (Kochkov et al. 2024; Zhang et al. 2025). In this study, we use the pre-trained 1.4° deterministic version following the configuration of Zhang et al. (2025).

ACE2

ACE2 (Ai2 Climate Emulator version 2, Watt-Meyer et al. 2025) is a 450-million-parameter autoregressive ML atmospheric emulator developed at the Allen Institute for Artificial Intelligence. The model operates at 1° horizontal resolution with eight terrain-following vertical layers and advances the atmospheric state forward in 6-hour increments. A distinguishing feature is its strict conservation of global dry air mass and total atmospheric moisture, which permits arbitrarily long stable integrations with a throughput of approximately 1500 simulated years per wall-clock day (Watt-Meyer et al. 2025). ACE2 accepts time-varying SST and CO_2 concentration as external boundary conditions, enabling it to respond to evolving ocean forcing and greenhouse gas changes—capabilities that represent key advances over its predecessor (Watt-Meyer et al. 2025). The model has been trained on either ERA5 reanalysis (ACE2-ERA5) or GFDL's SHiELD model output (ACE2-SHiELD), and has been shown to skillfully reproduce ENSO-driven atmospheric variability, long-term global temperature trends, and emergent features such as TC activity and the Madden–Julian Oscillation. In this study, we use the pre-trained ACE2-ERA5.

b. Experimental hindcast settings

Table 1 summarizes the experimental design of the nine seasonal prediction configurations compared in this study. These comprise the dynamical benchmark (SPEAR), the high-resolution dynamical model nudged toward SPEAR-predicted SST (HiFLOR-S), the AI-based atmospheric emulator ACE2-ERA5 forced by SPEAR-predicted SST and sea ice (ACE2_SPEAR), and six NeuralGCM-based configurations that differ only in the source of their prescribed SST and sea-ice boundary conditions.

These six NeuralGCM configurations otherwise share an identical model configuration (1.4° horizontal resolution, 32 vertical levels, ERA5-initialized atmosphere/land state, and a 1993–2025 evaluation period), so they are grouped under a single N_* column in Table 1. The forecast length, ensemble size, and SST/sea-ice source specific to each of the six configurations—named for that source (N_SPEAR, N_SEAS5, N_DWD, N_METFR, N_ECCC, N_CMCC)—are detailed separately in Table 2. This design isolates the effect of SST/sea-ice-forcing source on seasonal TC prediction skill while holding the underlying atmospheric model fixed. Conversely, forcing different models—HiFLOR-S, ACE2_SPEAR, and N_SPEAR—with the same SPEAR-predicted SST and sea ice also allows the models' differing responses to identical SST/sea-ice forcing to be evaluated. All configurations are initialized once per month; the AI-based configurations additionally draw ensemble members from a five-day lagged-ERA5 initial-condition cycle (Table 1, note b). The primary target season is July–November (JASON); we also evaluated May–November (MJJASON), with corresponding results presented in the supplemental material. Note that January and February initializations are unavailable for NeuralGCM because of computational instability associated with initialization in these months; the root cause of this instability remains under investigation. The forecast length and number of ensemble members of the NeuralGCM-based configurations also vary, reflecting differences in the availability of boundary-condition data from each forecast agency through the Copernicus Climate Change Service Climate Data Store dataset.

c. Evaluated TC variables, bias corrections, and skill metrics

Following the metric definitions of Murakami et al. (2016b, 2025), we evaluate tropical storms (TCS; sustained surface winds $\geq$ 17.5 m s^{-1}) and hurricanes (HUR; $\geq$ 32.9 m s^{-1}); storms of hurricane intensity are locally termed "typhoons" in the WNP, but for consistency we refer to them

Table 1. Experimental design of the seasonal hindcast configurations evaluated in this study. All configurations are initialized once per month and run as multi-member ensemble forecasts (ensemble size given below); the AI-based configurations additionally draw ensemble members from lagged atmospheric initial conditions[b] (see Atmosphere/land IC below). Other configuration details follow Murakami et al. (2025) for SPEAR and HiFLOR-S. "AI" denotes a machine-learning atmospheric emulator. Prescribed SST and sea-ice boundary conditions for the AI-based and HiFLOR-S configurations are taken from the predicted fields of the indicated source configuration; SPEAR is a fully coupled ocean–atmosphere model and requires no external SST/sea-ice forcing. Configuration-dependent TC detection criteria (T_a, SLP_a, and W_s, see Section 2d) are also listed. The six NeuralGCM-based configurations (N_SPEAR, N_SEAS5, N_DWD, N_METFR, N_ECCC, N_CMCC) are merged into a single N_* column; rows on which they differ are detailed in Table 2.

	SPEAR	HiFLOR-S	ACE2_SPEAR	N_* (SPEAR, SEAS5, DWD, METFR, ECCC, CMCC)
Base model	Dynamical (SPEAR)	Dynamical (HiFLOR)	AI (ACE2)	Hybrid (NeuralGCM)
Atmosphere resolution	50 km, C192 (33 levels)	25 km, C384 (33 levels)	1° (8 levels)	1.4° (32 levels)
Ocean resolution	100 km	100 km	none	none
Evaluation period	1993–2025	1993–2025	1993–2025	1993–2025
Initial month	1–12	1–8	1–8	3–8
Forecast lengths (months)	12	12	12	varies[c]
Ensemble members	30 (15 before Jun 2020)[d]	30 (15 before Jun 2020)[d]	30 (15 before Jun 2020)[d]	varies[c]
Atmosphere/land IC	SPEAR nudged (Lu et al. 2020)	SST-forced AMIP simulations	ERA5[b]	ERA5[b]
Ocean IC	SPEAR_ECDA (Lu et al. 2020)	none	none	none
Prescribed SST	None (fully coupled)	SPEAR predicted[a]	SPEAR predicted	varies[c]
Prescribed sea ice	None (fully coupled)	None (interactive)[e]	SPEAR predicted	varies[c]
TC Detection Criteria (T_a, SLP_a, W_s)	1K, −2 hPa, 15.75 m s^{-1}	2K, −2 hPa, 17.5 m s^{-1}	0.5K, −1 hPa, 10.75 m s^{-1}	0.25K, −0.5 hPa, 10.75 m s^{-1}

[a] 5-day nudging toward SPEAR-predicted SST (Murakami et al. 2025).
[b] Lagged ERA5 analyses (Hersbach et al. 2020) spanning the five days up to and including the 1st of the initialization month: member 1 uses the 1st-day analysis, member 2 the previous day, . . . , member 5 four days prior; the 5-day cycle then repeats for additional members (e.g., member 6 again uses the 1st-day analysis).
[c] Differs among the six N_* configurations by prescribed SST source; see Table 2.
[d] Fifteen members for forecasts initialized before June 2020 and 30 for initializations from June 2020 onward, reflecting an expansion of GFDL's real-time SPEAR ensemble.
[e] Simulated interactively by HiFLOR-S's own coupled ocean–ice component, not taken from SPEAR (Murakami et al. 2025).

as "hurricanes" throughout this study. We further quantify Accumulated Cyclone Energy (ACE), the lifetime sum of squared maximum sustained wind speed scaled by 10^{-5} (units of 10^5 m^2 s^{-2}; Bell et al. 2000). Skill is assessed for the interannual variability of basin-total TCS, HUR, and

TABLE 2. Configuration details that differ among the six NeuralGCM-based configurations merged into the N_* column of Table 1, which otherwise share an identical model configuration (1.4°, 32 levels; no interactive ocean; ERA5[b] atmosphere/land initial conditions; 1993–2025 evaluation period; initial months 3–8). Configurations are named for the source of their prescribed SST and sea-ice boundary conditions (Table 1). Where two ensemble sizes are given, the second is the current size and the first applied to initializations before the indicated month, following an expansion of the corresponding agency's operational seasonal forecast ensemble.

	N_SPEAR	N_SEAS5	N_DWD	N_METFR	N_ECCC	N_CMCC
Forecast lengths (months)	12	7	6	7	7	6
Ensemble members	30 (15 before Jun 2020)	51 (25 before Jan 2017)	50 (30 before Jan 2024)	51 (31 before Jan 2025)	20	50 (30 before Jan 2025)
Prescribed SST & sea ice	GFDL (SPEAR) predicted	ECMWF (SEAS5) predicted	DWD (GCFS2.2) predicted	Météo-France (System 9) predicted	ECCC (CanESM5.1p1bc, GEM5.2-NEMO) predicted	CMCC (CM3) predicted

ACE across three ocean basins: Western North Pacific (WNP), Eastern North Pacific (ENP), and North Atlantic (NA) (basin boundaries shown in Fig. 1). Because each configuration exhibits systematic biases in its predicted values relative to observations, ensemble forecasts for these TC metrics were calibrated following Murakami et al. (2016b, 2025): the predicted value for each ensemble member was scaled by the ratio of the observed to the predicted ensemble-mean value over the period 1993–2025. This bias correction ensures that the predicted climatology matches the observed climatology, allowing skill assessment to focus on interannual variability rather than absolute bias. We additionally examine TC frequency of occurrence (TCF), the density of 6-hourly TC positions within $2.5° \times 2.5°$ grid cells (Murakami et al. 2020, 2025). Similarly, TC genesis frequency (TGF) is computed using the same method but restricted to each storm's genesis position rather than its full 6-hourly track.

Two complementary metrics, adopted from Murakami et al. (2016b, 2025), quantify skill relative to observations: the Spearman rank correlation (RCOR) and the mean squared skill score (MSSS) (Kim et al. 2012; Li et al. 2013). As in Vecchi et al. (2014), we rely on rank rather than Pearson correlation because neither the (generally non-integer) ensemble-mean predicted TC counts nor the observed annual counts, which are integers, can be assumed Gaussian, and because Pearson correlation is easily distorted by the occasional extreme value characteristic of TC records. RCOR instead measures the degree to which the forecast reproduces the observed rank ordering of years from quietest to most active, without assuming a particular underlying distribution. MSSS, by contrast, benchmarks forecast error against a climatological reference, with positive values denoting skill that exceeds climatology. We assess the statistical significance of RCOR using a two-tailed test with the effective sample size reduced for lag-1 autocorrelation in both series (following Bretherton et al. 1999, their Eq. 31).

d. TC detection methods

TCs from configuration outputs were identified using the objective tracking algorithm developed by Harris et al. (2016) and subsequently applied in Murakami et al. (2015). The algorithm detects candidate TCs as coherent regions enclosed by negative sea level pressure anomaly (SLP_a) contours that are collocated with a warm-core temperature anomaly (T_a). To be classified as a TC, a candidate storm must retain its warm-core structure for at least 36 h and satisfy the prescribed maximum sustained surface wind speed threshold (W_s).

For SPEAR and HiFLOR-S, the detection thresholds were retained from earlier studies (Murakami et al. 2015, 2016b, 2020, 2025). These thresholds were originally selected to compensate for differences in configuration resolution and intensity representation while yielding a realistic global climatology of approximately 80–90 TCs per year. Because comparable detection criteria are not available for the AI-based configurations, the SLP_a, T_a, and W_s thresholds for ACE2 and NeuralGCM were calibrated preliminarily through a series of sensitivity tests designed to reproduce a similar climatological TC frequency. The final threshold values adopted for each configuration are summarized in Table 1.

e. Observational and reanalysis datasets

The observed TC "best-track" data for the period 1993–2025 were obtained from the International Best Track Archive for Climate Stewardship (IBTrACS v04r01; Knapp et al. 2010). We used a compilation from the National Hurricane Center and Joint Typhoon Warning Center, identified by the flag "usa" in the IBTrACS dataset. We considered TCs of tropical storm intensity or greater, defined as those with 1-minute sustained surface winds of 17.5 m s^{-1} or greater. The large-scale variables used in the genesis-environment diagnostics of Section 2f are derived from the Japanese Reanalysis for Three Quarters of a Century (JRA-3Q) dataset (Kosaka et al. 2024), interpolated onto the same $2.5° \times 2.5°$ grid used for TGF.

f. Large-scale genesis environment diagnostics

We evaluate six large-scale variables relevant to TC genesis. Three are thermodynamic: SST (K), relative humidity at 600 hPa (RH_{600}, %), and maximum potential intensity (MPI, m s^{-1}; Bister and Emanuel 1998). Three are dynamical: vertical wind shear between 200 and 850 hPa (V_s, m s^{-1}), 850-hPa relative vorticity (ζ_{850}, s^{-1}), and the meridional shear of the 500-hPa zonal wind (U_y, s^{-1}; Wang and Murakami 2020). These variables are regarded as important for TC genesis and are commonly included in the tropical cyclone genesis potential index (e.g., Gray 1979; Emanuel and Nolan 2004; Tippett et al. 2011; Tang and Emanuel 2012; Wang and Murakami 2020; Murakami and Wang 2022). The same six variables were computed from each hindcast configuration's own output on pressure levels. We originally intended to include 500-hPa vertical velocity (ω_{500}), as reported in Wang and Murakami (2020), among these variables, but this field is not supported in NeuralGCM's output and is therefore excluded. For ACE2_SPEAR, these fields are obtained by vertical interpolation from the eight native vertical layers of ACE2_SPEAR, so the interpolated fields—particularly the upper-tropospheric (200-hPa) winds entering the vertical wind shear V_s—may be subject to additional uncertainty.

We evaluate four aspects of the large-scale genesis environment, for the July-initialized, July–November season, 1993–2025 (33 yr). At the grid-point scale, we examine the climatological pattern of TGF and TC-genesis sensitivity to large-scale conditions. At the sub-basin scale, we examine the interannual skill of those conditions and TC-genesis sensitivity to them. First, at every $2.5° \times 2.5°$ grid cell, we compute the spatial pattern correlation (R) and RMSE between each configuration's 1993–2025 climatological mean TGF and observations. We also identify which of the six large-scale variables' interannual time series most strongly correlates with that configuration's own interannual TGF at that point, collapsed to a binary thermodynamic-versus-dynamical category. Second, for six sub-basin main development regions (MDRs, defined in Section 3), we correlate each configuration's own area-averaged interannual series of each large-scale variable against JRA-3Q. From each configuration's own fields, we separately identify which variable is most strongly correlated with its own box-averaged TGF variability. Grid points where a configuration's own TGF has zero interannual variance are excluded from the dominant-driver diagnostic. Because TGF is a small, often near-zero interannual count, all interannual correlations involving TGF or the large-scale variables use the RCOR, with significance assessed by a two-tailed t-test on the effective sample size reduced for lag-1 autocorrelation.

3. Results

a. Climatological TC characteristics from hindcasts

Before assessing detailed prediction skill, we first examine the climatological TC characteristics of each configuration's hindcasts. Figure 1 compares the hindcast TC tracks against IBTrACS observations over the verification period. The configurations generally reproduce the observed TC climatology, although some systematic biases are evident. For instance, SPEAR and HiFLOR-S tend to overestimate TC frequency in the WNP and underestimate it in the NA, whereas the NeuralGCM- and ACE2-based configurations show weaker biases. SPEAR-predicted SST was also prescribed for N_SPEAR and ACE2_SPEAR, yet the systematic biases seen in SPEAR and HiFLOR-S are absent from these two configurations. This indicates that the WNP and NA biases in SPEAR and HiFLOR-S do not arise directly from errors in the predicted SST field, but instead likely reflect the configurations' own physics, independent of the prescribed SST forcing. Although the horizontal resolution of ACE2 (1°) is finer than that of NeuralGCM (1.4°), ACE2_SPEAR simulates almost no hurricanes, whereas NeuralGCM produces them. This contrast suggests that horizontal resolution alone does not explain the ability of these models to represent hurricane-strength TCs. Instead, it may reflect differences in how the models represent the dynamical and thermodynamic structure of TCs, including their warm-core structure. The NeuralGCM-based configurations show similar track distributions, although the N_DWD and N_METFR configurations produce slightly more TCs in the WNP than N_CMCC and N_ECCC. The differences among the six NeuralGCM-based configurations may mostly stem from their prescribed SST and sea-ice boundary conditions, which are derived from different forecast agencies (Table 2), although internal atmospheric variability may also contribute. Overall, these results suggest that although all configurations capture the broad climatological features of TC activity, systematic biases persist that may affect their seasonal prediction skill.

Figure 2 compares the climatological annual cycle of TC genesis frequency. Overall, the seasonal timing of genesis is reproduced in all ocean basins. Most of the nine hindcast configurations track the observed July–October single peak in the WNP, ENP, and NA. In general, the NeuralGCM-based

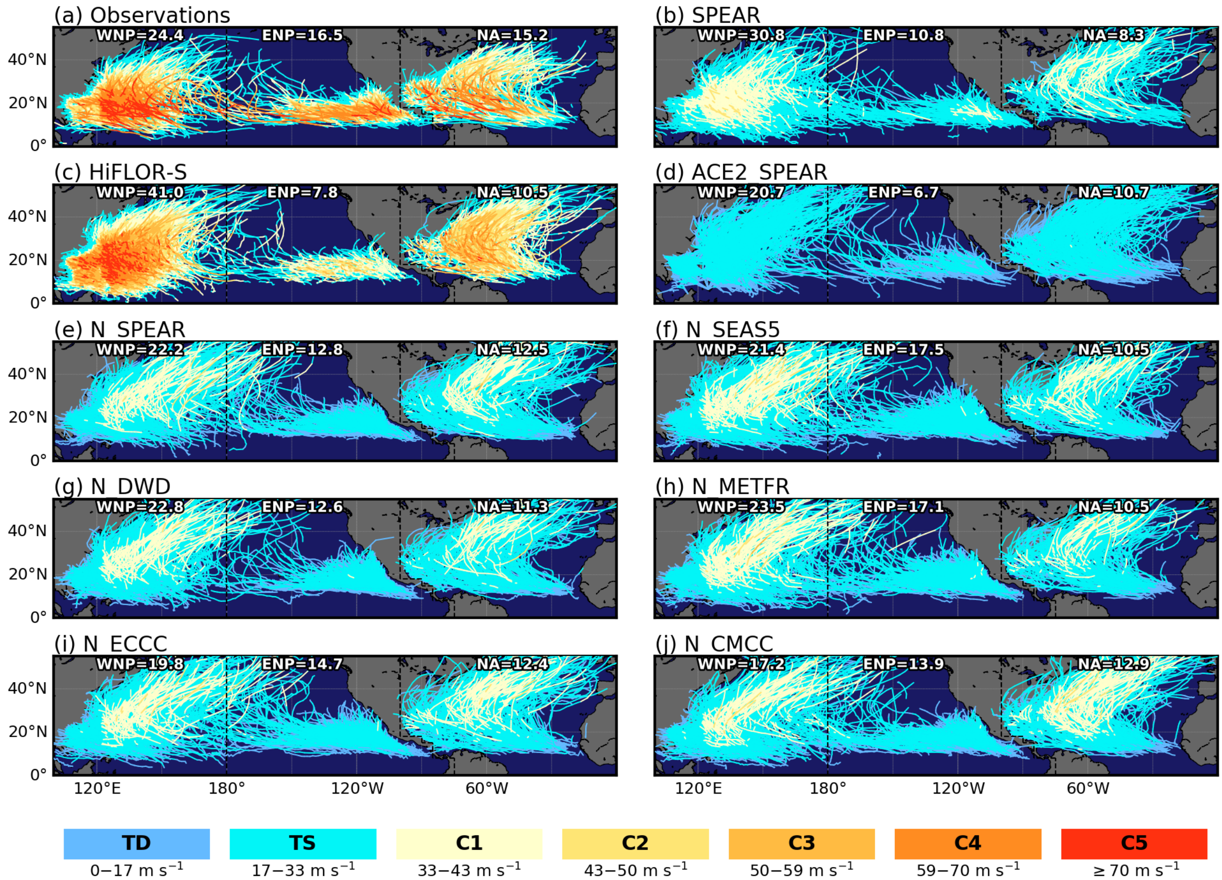

FIG. 1. TC tracks, March–December, 1993–2025, for (a) observations and (b)–(j) the nine hindcast configurations, as labeled (Table 1). For each hindcast configuration, tracks are taken from the March initialization (genesis months March–July) concatenated with the August initialization (genesis months August–December) to give continuous March–December coverage, using ensemble member 1 only; the observed tracks are filtered to the same March–December genesis window. Track segments are colored by the maximum sustained surface wind speed at each 6-hourly position: tropical depression (TD, < 17 m s^{-1}), tropical storm (TS, 17–33 m s^{-1}), and Categories 1–5 (C1–C5; 33–43, 43–50, 50–59, 59–70, and ≥ 70 m s^{-1}, respectively). Dashed black lines mark the boundaries of the three verification basins used throughout this study: WNP, ENP, and NA. The white number with black outline in each basin gives the 1993–2025 climatological annual-mean TC genesis count for that basin.

configurations show a similar seasonal cycle across the six prescribed-SST configurations. However, there are some biases specific to a configuration and ocean basin. For example, HiFLOR-S

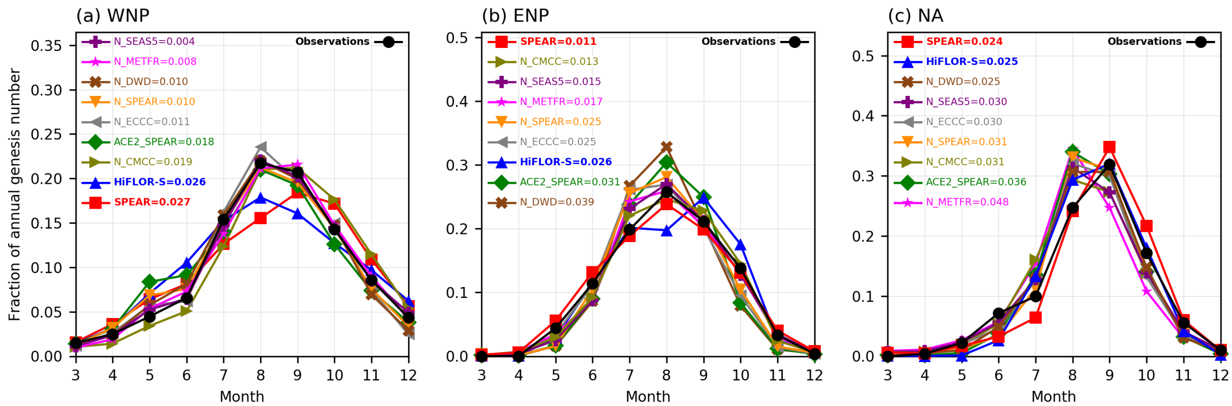

FIG. 2. Climatological annual cycle of TC genesis frequency, March–December, 1993–2025, for (a) WNP, (b) ENP, and (c) NA, comparing IBTrACS observations (black) against the nine hindcast configurations, each shown with a distinct color and marker. For each hindcast configuration and each target month, the genesis count is pooled over every initialization whose forecast lead reaches that month—including, for the four 12-month-lead configurations (SPEAR, HiFLOR-S, ACE2_SPEAR, N_SPEAR), initializations that reach the target month via a lead that crosses into the following calendar year—and over all ensemble members of that configuration (Table 2); observations have no initialization/ensemble dependence and use the 33-yr mean genesis count for each calendar month directly. Within each basin panel, every configuration's 10 monthly values (March–December) are normalized to sum to 1, so the curves compare the seasonal *timing* of genesis independent of each configuration's overall annual TC frequency. The value next to each configuration's line-and-marker key gives the root-mean-square error (RMSE) of its normalized seasonal cycle against observations, listed from smallest (best agreement, top) to largest.

and SPEAR show the largest root-mean-square error (RMSE) in the WNP among the nine configurations, whereas they show the smallest RMSE in the NA. In the ENP and NA, most configurations reproduce the single midsummer-to-early-autumn peak; however, all AI configurations simulate a peak season one month earlier than the observed peak in the NA, with only SPEAR reproducing the September peak.

b. Correlation skill in basin-total TC metrics

First, we evaluate prediction skill in basin-total TC metrics for each configuration. Figure 3 shows interannual time series of July- and June-initialized basin-total TCS predictions over the NA,

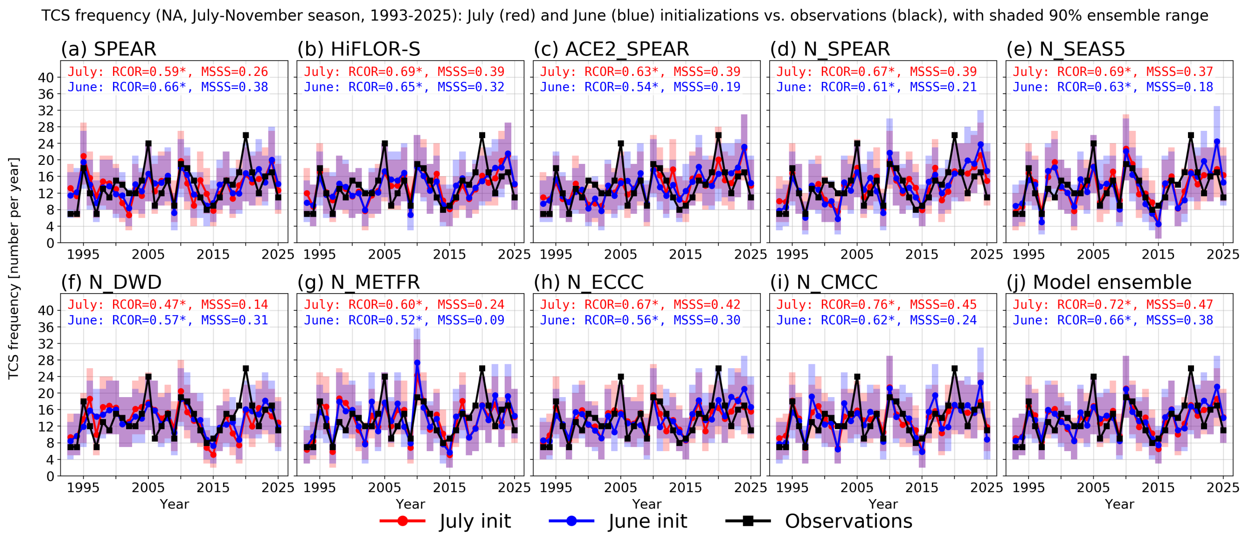

FIG. 3. Time series of observed and predicted seasonal (July–November) TCS over the NA, 1993–2025, for (a)–(i) the nine hindcast configurations, as labeled, and (j) a multi-model ensemble formed by pooling every ensemble member from the nine configurations in (a)–(i). In each panel, observations (IBTrACS; black) are compared against two initializations of the same configuration: the July initialization (lead month 0; red) and the June initialization (lead month 1; blue); panel (j) pools the July-initialized members of all nine configurations (red) and, separately, the June-initialized members of all nine configurations (blue). Shading gives the 90% range of the ensemble, computed from a Poisson distribution with rate equal to the ensemble-mean TCS in that year. RCOR and MSSS for each initialization are given as text in each panel (asterisk: significant at $p < 0.05$, two-sided test).

evaluated against IBTrACS observations for the July–November season, 1993–2025. Figures S1 and S2 show the corresponding time series for the WNP and ENP, respectively.

For the July initialization (lead month 0), RCOR ranges from 0.47 (N_DWD) to 0.76 (N_CMCC) across the nine hindcast configurations, MSSS from 0.14 to 0.45 (Fig. 3); MSSS is positive and RCOR significant ($p < 0.05$) for every configuration. Seven of the other eight configurations (ACE2_SPEAR, HiFLOR-S, and five of the six NeuralGCM configurations) meet or exceed the July-initialized RCOR of the semi-operational dynamical benchmark SPEAR (0.59); only N_DWD (0.47) falls clearly below it, while N_METFR (0.60) is essentially comparable.

Skill at the one-month-earlier June initialization (lead month 1, blue) is generally lower than at the July initialization, as expected for the longer lead time. June-initialized RCOR (MSSS) ranges from 0.52 (0.09) for N_METFR to 0.66 (0.38) for SPEAR, and remains significant at $p < 0.05$ for every configuration (Fig. 3). Two configurations depart from this expected lead-time ordering: SPEAR and N_DWD both score higher from the June initialization than from July (SPEAR: RCOR 0.59→0.66, MSSS 0.26→0.38; N_DWD: RCOR 0.47→0.57, MSSS 0.14→0.31). We do not have an established explanation for this reversal; it may reflect a genuine seasonal-timing effect specific to these two configurations, or sampling variability given the 33-yr record.

Because EnsMean pools only the configurations with valid data at each lead, its composition narrows from all nine configurations at 0–2-month lead to the four 12-month configurations at 3–6-month lead, and it tracks near the top of the range at short lead without consistently being the single best configuration. Pooling every member from all nine configurations (Fig. 3j) matches SPEAR, the best individual configuration, on both metrics for June (RCOR 0.66, MSSS 0.38) and achieves the highest July MSSS (0.47 vs. N_CMCC's 0.45), though its July RCOR (0.72) remains second to N_CMCC's (0.76). This asymmetry reflects how equal-weight pooling operates. Pooling mainly reduces the variance component of forecast error, which lowers MSE (and raises MSSS) largely independent of which members are skillful. It does not reduce RCOR in the same guaranteed way, however, since RCOR depends on relative year-to-year ordering rather than error variance: diluting one configuration's well-timed signal (e.g., N_CMCC's) with differently timed signals from the rest can leave the pooled ranking below the single best-performing configuration even as its MSE stays lowest. We revisit this pooling behavior later in this section.

Figure 4 assesses whether the patterns identified above for NA TCS generalize across basins, metrics, and the full range of lead times. It shows RCOR for every combination of configuration, lead (0–6 months), TC metric (TCS, HUR, ACE), and basin (NA, WNP, ENP). Figure S3 shows the corresponding heatmap for the May–November forecasts.

Skill is highest and most consistently significant at short leads (0–2 months) across nearly every configuration, metric, and basin. Beyond 2-month lead, only four of the nine configurations—SPEAR, HiFLOR-S, ACE2_SPEAR, and N_SPEAR—have forecasts long enough to be evaluated for the July–November season (Table 2). The other five NeuralGCM configurations (N_SEAS5, N_METFR, N_ECCC: 7-month forecasts; N_DWD, N_CMCC: 6-month forecasts) run out of season coverage by 1- or 2-month lead, leaving those cells blank in Fig. 4—a data-availability limit rather than a skill degradation.

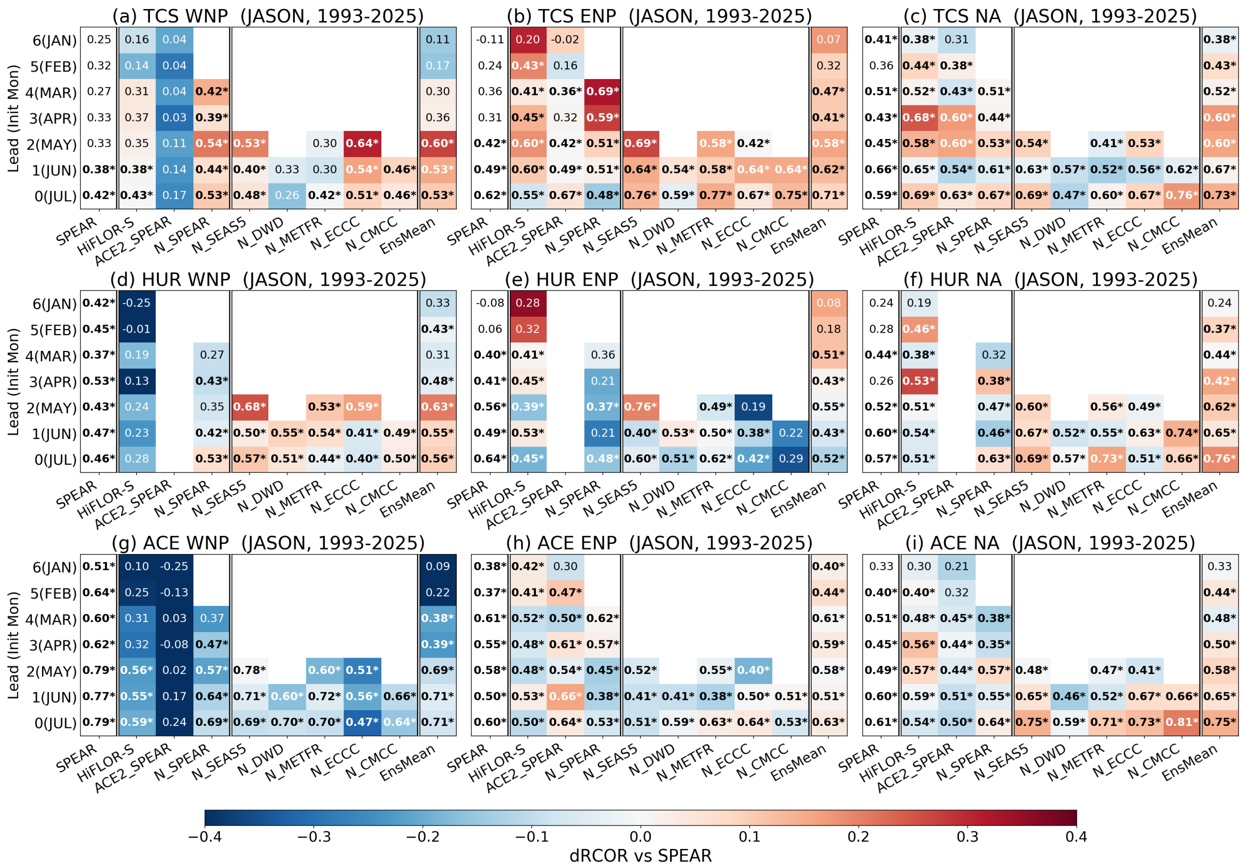

FIG. 4. RCOR between predicted and observed basin-total seasonal (July–November, JASON, 1993–2025) (a–c) TCS, (d–f) HUR, and (g–i) ACE, for lead times of 0 (July initialization) through 6 (January initialization) months, over (a,d,g) WNP, (b,e,h) ENP, and (c,f,i) NA. Columns give the nine hindcast configurations of Table 1 plus a multi-model ensemble (EnsMean) formed by pooling every ensemble member from all nine configurations with equal weight. The number in each cell is that configuration's own RCOR against observations; bold with an asterisk denotes significant RCOR at $p < 0.05$ using a two-tailed test. Shading gives the difference in RCOR from SPEAR (red: configuration exceeds SPEAR, blue: configuration trails SPEAR); the SPEAR column itself has a white background. Blank cells indicate a lead/configuration combination without hindcast data. For ACE2_SPEAR in HUR (d–f), every lead is blank because ACE2_SPEAR produces effectively no hurricane-intensity storms (Fig. 1d), leaving no valid series to correlate.

Among the four configurations evaluable at 3–6-month lead, N_SPEAR stands out: it frequently matches or exceeds SPEAR's own skill at these extended leads, particularly in WNP and ENP, where SPEAR's own correlation has already decayed to non-significance. At 4-month lead (March initialization) in TCS, for example, N_SPEAR remains significant in WNP (RCOR 0.42) and ENP

(0.69) while SPEAR does not (WNP 0.27, ENP 0.36); the same pattern holds at 3-month lead (April) in ENP (N_SPEAR 0.59 vs. SPEAR 0.31). In NA, by contrast, SPEAR itself remains significant at every lead through 4 months (Fig. 4c), consistent with the lead-time reversal noted above being specific to NA.

Two metric-specific contrasts stand out. ACE2_SPEAR's HUR correlation is undefined at every lead and basin because the configuration produces effectively no hurricane-intensity storms, consistent with the climatological track behavior shown in Fig. 1d. The same limitation depresses its ACE skill specifically in WNP, where ACE2_SPEAR is the only configuration that never reaches significance across all seven leads (RCOR between −0.25 and 0.24), even though its skill in the other ocean basins is comparable to the other configurations at short lead. Conversely, SPEAR itself is the standout performer for ACE in WNP (RCOR 0.51–0.79, significant at every evaluable lead)—the one basin/metric combination in which no other configuration matches the dynamical benchmark.

Because the top-performing configurations' RCOR differs by only 0.05–0.15 within this 33-yr record, selecting or upweighting only the most skillful configurations, rather than pooling all nine as EnsMean does, is a natural alternative worth testing, but doing so risks overestimating skill through selection bias unless evaluated out of sample. Leave-one-year-out cross-validation shows that no single subset size is uniformly better than pooling all nine configurations: the best subset size varies unpredictably by basin and initialization month, so a skill-based subset is not a reliably better strategy than the uniform pooling used for EnsMean throughout this section (see Supplementary Results S1 for the full analysis).

Because ACE2 and NeuralGCM were themselves trained on ERA5 spanning parts of the verification period (Watt-Meyer et al. 2025; Kochkov et al. 2024), we repeated the verification restricted to years outside any training or validation use (n = 14 for ACE2_SPEAR, n = 7 for the NeuralGCM-based configurations; Figs. S7–S8). Skill rankings are largely preserved (63–65% of cells retain the same sign of ΔRCOR; qualitative reversals occur in only 11–15%), with no evidence that training overlap explains the AI-based configurations' competitiveness with SPEAR. The one notable exception is ACE2_SPEAR's WNP TCS skill at long leads, where SPEAR's own out-of-sample correlation happens to weaken within this smaller sample; ENP TCS skill, by contrast, remains high and significant out of sample for most NeuralGCM-based configurations (RCOR up to 0.90).

c. Sub-basin spatial skill

While Section 3b evaluated basin-total skill, such aggregate diagnostics cannot indicate where within a basin a configuration is skillful. We therefore also evaluate forecast skill at the sub-basin (grid-point) scale, following Murakami et al. (2016b, 2025). We compute the RCOR between the ensemble-mean forecast and observed TCF at every grid box over the 1993–2025 hindcast period (33 years), separately for each initialization lead and for the TCS (all tropical storms) and HUR (hurricane-intensity, ≥C1) categories.

Figure 5 maps the July-initialized (0-month lead), July–November season grid-point RCOR for TCS for all nine individual configurations (panels a–i) and multi-model mean (panel j). Figure S4 shows the corresponding skill map for HUR. Figures S5 and S6 show the corresponding skill maps for May–November forecasts from the May initializations. We restrict the evaluation domain at every grid box to locations where TC occurrence is recorded in at least 25% of the 33 years.

All configurations reproduce a broadly similar large-scale pattern of significant positive skill across the WNP (120°E–180°) and the eastern-to-central ENP, with weaker and more spatially patchy skill over the NA main development region. Within this shared pattern, however, the configurations differ systematically by basin. SPEAR (Fig. 5a) shows the most spatially extensive significant skill in the WNP of any single configuration. In the ENP and NA, by contrast, every NeuralGCM-based configuration and ACE2_SPEAR shows visibly more extensive significant, positive skill than SPEAR, particularly along the eastern Pacific ITCZ region and in the western tropical Atlantic/Caribbean.

Figure 6 quantifies significant-skill area (percentage of the observation-testable domain, shaded by its difference from SPEAR). Three points emerge. First, the WNP is the one basin where SPEAR remains competitive with or exceeds most NeuralGCM-based configurations at short lead (e.g., TCS WNP, 0-month lead: SPEAR 47% vs. 37–46%), consistent with Fig. 5. ACE2_SPEAR is a clear outlier there, with substantially smaller significant area than every other configuration across all leads. Second, in the ENP and NA the sign flips: nearly every AI-based configuration exceeds SPEAR at every lead for which it has data, by as much as 20–25 percentage points in TCS and a comparable margin in HUR. Third, skill decays with lead time and the AI-based advantage in the ENP/NA generally narrows (TCS) or becomes mixed (HUR), though the number of configurations

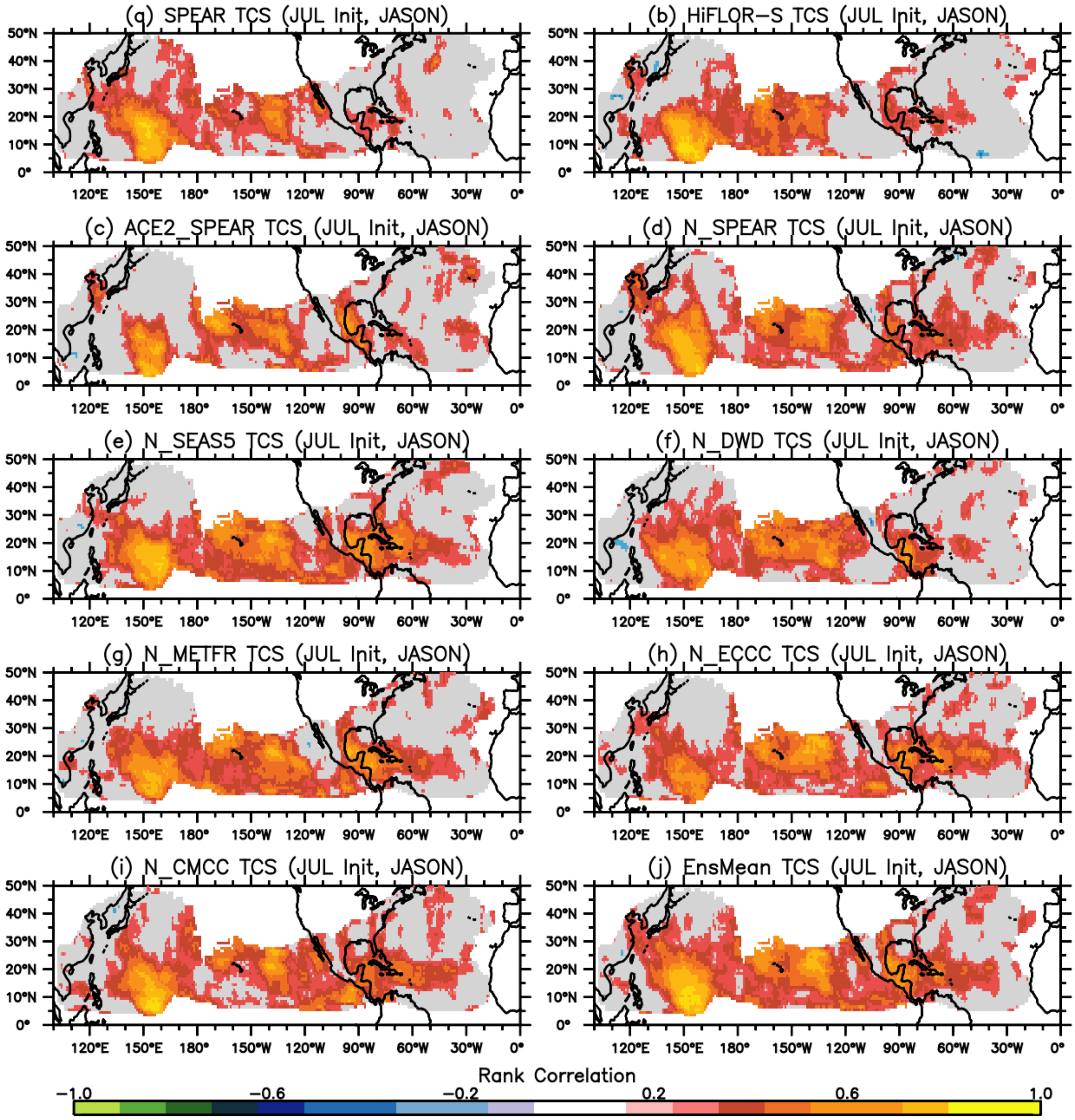

FIG. 5. Grid-point RCOR skill for TC frequency of occurrence (all TCS), July-initialized (0-month lead) forecasts of July–November-season activity, 1993–2025 (33 years), for (a) SPEAR, (b) HiFLOR-S, (c) ACE2_SPEAR, (d) N_SPEAR, (e) N_SEAS5, (f) N_DWD, (g) N_METFR, (h) N_ECCC, (i) N_CMCC, and (j) multi-model mean (EnsMean). Colored shading shows the RCOR between ensemble-mean forecast and observed TCF at each grid box, where statistically significant at $p \leq 0.1$; gray shading indicates grid boxes with observed TC activity in $\geq$25% of the 33 years but no significant forecast skill; unshaded (white) regions have insufficient observed TC activity to test (<25% of years).

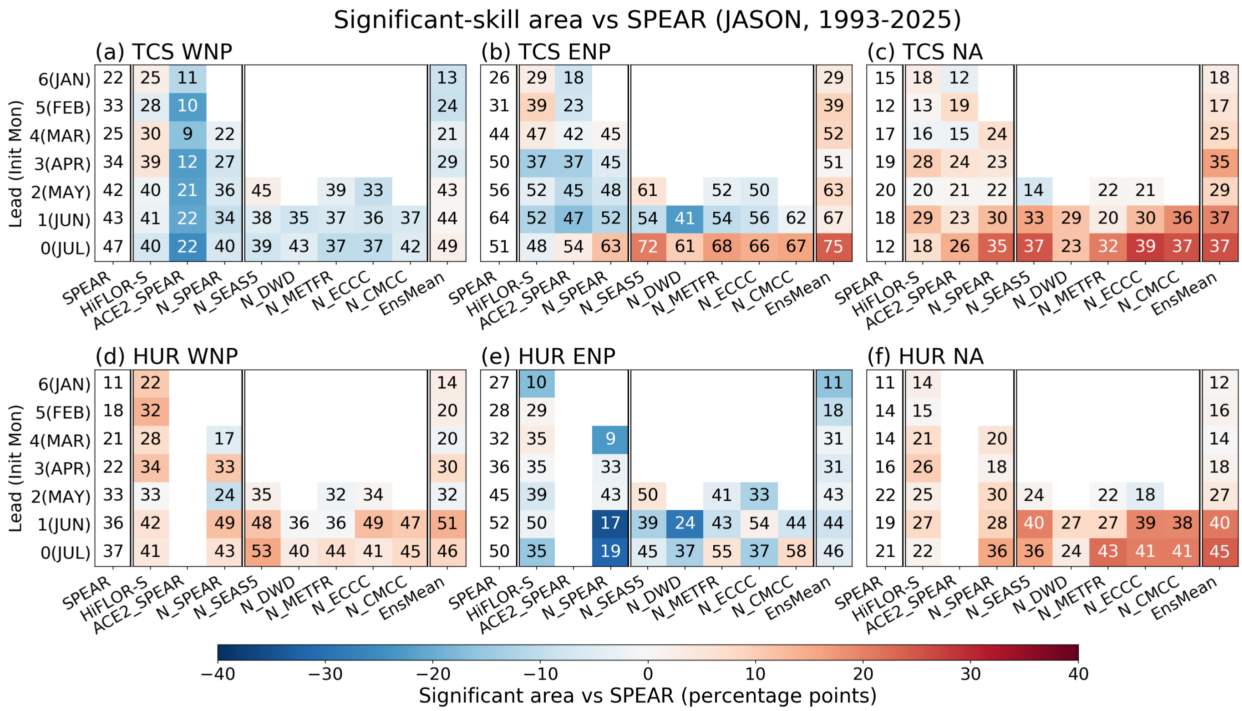

FIG. 6. Basin-scale summary of grid-point skill for TC frequency of occurrence, as the percentage of the observation-testable domain (basin ∩ grid boxes with ≥25% active years; e.g., gray domain in Fig. 5) with statistically significant RCOR, for TCS (a–c) and HUR (d–f) in the (a,d) WNP, (b,e) ENP, and (c,f) NA, 1993–2025. Rows show the seven initialization leads (0–6 months; July–January). Columns show the nine hindcast configurations and EnsMean, as labeled (Table 1). Cell shading shows each configuration's significant-skill-area percentage minus SPEAR's at the same lead/basin/category (red: larger than SPEAR; blue: smaller); cell numbers give each configuration's own significant-skill-area percentage relative to the observation-testable area. ACE2_SPEAR is excluded from EnsMean in the HUR panels (d–f) because it produces effectively no hurricane-intensity storms.

still producing forecasts also shrinks at long leads (Table 2). EnsMean generally shows either the highest skill of all configurations or skill competitive with the best individual one.

EnsMean's benefit relative to SPEAR is basin- and category-dependent rather than uniform. EnsMean exceeds SPEAR only marginally in the WNP (TCS, 0-month lead: 49% vs. 47%) because ACE2_SPEAR's low WNP skill pulls the pooled mean down. It is the best-performing configuration in the ENP (75% vs. SPEAR's 51% and the best individual configuration's 72%), as expected from classical ensemble averaging. In the NA its advantage over SPEAR (37%

vs. 12%) is slightly exceeded by the best individual configuration (N_ECCC, 39%). This TCS benefit does not carry over to HUR. EnsMean can trail both SPEAR and several individual AI-based configurations simultaneously in the ENP (0-month lead: 46% vs. SPEAR's 50% and N_CMCC's 58%). HUR is a rare-event category in which configurations often disagree on which years were locally active, so averaging dilutes rather than reinforces skill. EnsMean is therefore not a general-purpose improvement over the single best available configuration, particularly for hurricane-intensity storms.

d. Skill in large-scale environments related to TC genesis

Section 3b and Fig. 4 show that the nine hindcast configurations differ substantially in skill at predicting basin-total TC activity, but that comparison alone cannot distinguish two different sources of skill (Section 1; Murakami et al. 2025). One is whether a configuration's genesis variability responds correctly to a well-predicted large-scale environment. The other is whether apparently skillful TC statistics arise despite an unrealistic or only coincidentally correct representation of that environment. Departures from either may help explain the basin- and configuration-dependent skill differences. We evaluate four aspects of the large-scale genesis environment at two spatial scales, following the diagnostics described in Section 2f. They are the grid-point climatological pattern of TGF and TC-genesis sensitivity to large-scale conditions (Fig. 7), and the sub-basin interannual skill of those conditions and TC-genesis sensitivity to them (Fig. 8).

All nine configurations reproduce the observed climatological TGF spatial pattern with generally high fidelity (pattern correlation R = 0.84–0.92 in the WNP, 0.85–0.98 in the ENP; Fig. 7, left column). HiFLOR-S is an exception, substantially overestimating the climatological TGF in the WNP. RMSE for HiFLOR-S is twice as large as the other eight configurations. Pattern skill in TGF is more variable over the NA (R = 0.66–0.89). However, most configurations simulate higher TGF over the N2 domain than the N1 domain relative to observations, reflecting a common bias among dynamical models of underestimating TGF over the Caribbean Sea and Gulf of Mexico (e.g., Chu et al. 2026).

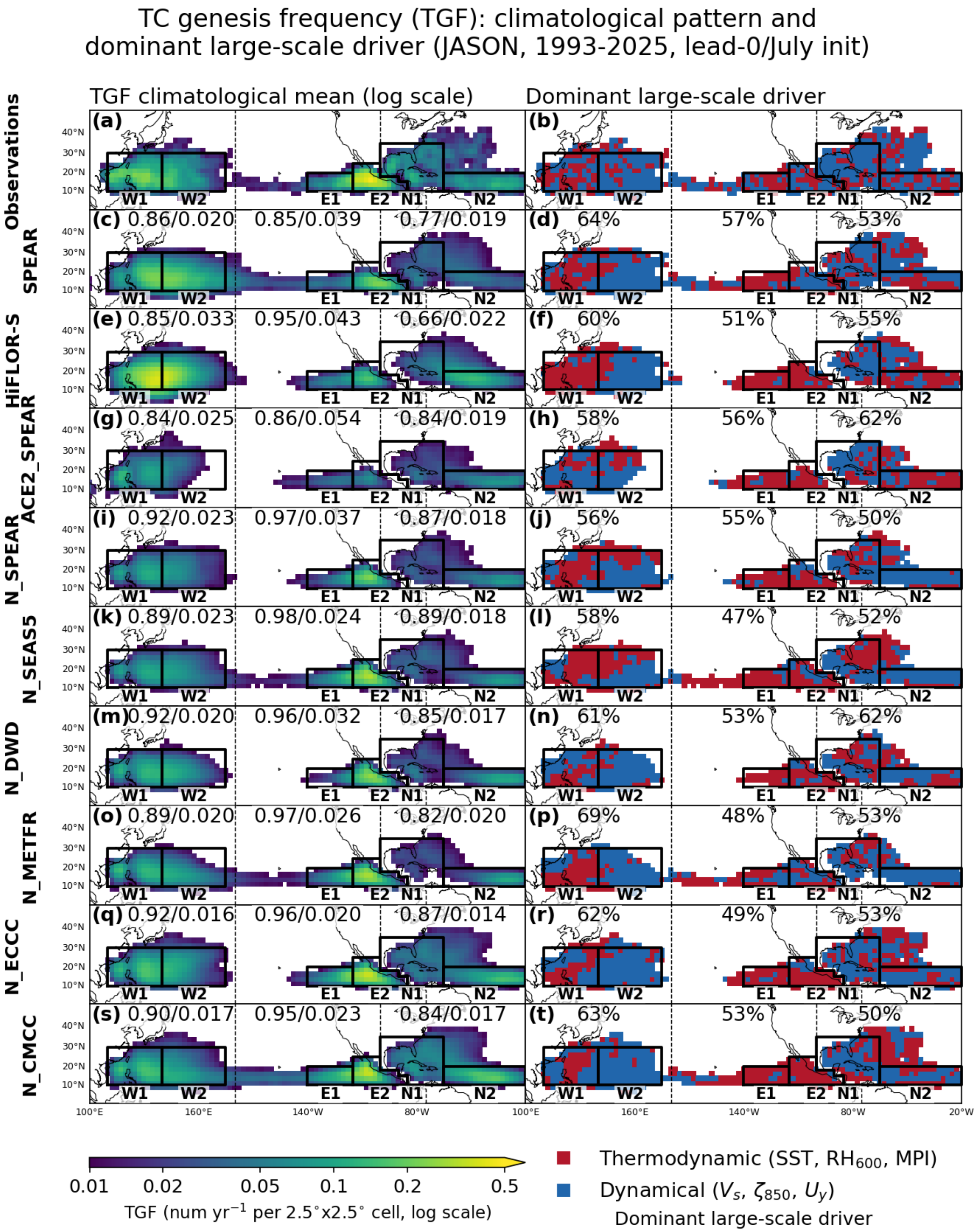
TC genesis frequency (TGF): climatological pattern and
dominant large-scale driver (JASON, 1993-2025, lead-0/July init)
TGF climatological mean (log scale)
Dominant large-scale driver
Observations
SPEAR
HiFLOR-S
ACE2_SPEAR
N_SPEAR
N_SEAS5
N_DWD
N_METFR
N_ECCC
N_CMCC
(a)
(b)
(c) 0.86/0.020 0.85/0.039 0.77/0.019
(d) 64% 57% 53%
(e) 0.85/0.033 0.95/0.043 0.66/0.022
(f) 60% 51% 55%
(g) 0.84/0.025 0.86/0.054 0.84/0.019
(h) 58% 56% 62%
(i) 0.92/0.023 0.97/0.037 0.87/0.018
(j) 56% 55% 50%
(k) 0.89/0.023 0.98/0.024 0.89/0.018
(l) 58% 47% 52%
(m) 0.92/0.020 0.96/0.032 0.85/0.017
(n) 61% 53% 62%
(o) 0.89/0.020 0.97/0.026 0.82/0.020
(p) 69% 48% 53%
(q) 0.92/0.016 0.96/0.020 0.87/0.014
(r) 62% 49% 53%
(s) 0.90/0.017 0.95/0.023 0.84/0.017
(t) 63% 53% 50%
W1 W2 E1 E2 N1 N2
40°N 30°N 20°N 10°N
100°E 160°E 140°W 80°W 100°E 160°E 140°W 80°W 20°W
0.01 0.02 0.05 0.1 0.2 0.5
TGF (num yr^{-1} per 2.5°x2.5° cell, log scale)
Thermodynamic (SST, RH_{600}, MPI)
Dynamical (V_s, ζ_{850}, U_y)
Dominant large-scale driver

FIG. 7. Climatological pattern and dominant driver of TGF, July–November (JASON), 1993–2025 July-initialized (0-month lead), for (a,b) observations and (c–t) the nine hindcast configurations, each shown as a pair of panels. Left-column panels show the climatological-mean TGF with log color scale; inset text gives the pattern correlation (R) and root-mean-square error against observations for the WNP, ENP, and NA basins. Right-column panels show, at every $2.5° \times 2.5°$ grid cell, which of six large-scale variables—SST, RH_{600}, MPI, V_s, ζ_{850}, and U_y—has the highest-magnitude RCOR with that configuration's own interannual TGF, collapsed to thermodynamic (SST, RH_{600}, MPI; red) or dynamical (V_s, ζ_{850}, U_y; blue); inset text gives the percentage of domain grid points at which that configuration's dominant category matches observations. Black boxes and labels (W1, W2 in WNP; E1, E2 in ENP; N1, N2 in NA) mark the six sub-basin main development regions (MDR) used for the box-averaged diagnostics of Fig. 8.

Thermodynamic skill is generally high. SST and MPI are predicted with mostly significant skill by every configuration in every basin (JRA-3Q-relative RCOR mostly 0.6–0.9; Fig. 8a–c), with the exception of MPI in the NA, where N_DWD (RCOR 0.22) and N_METFR (0.30) fall short of significance. Configurations show higher skill than SPEAR in predicting RH_{600} in the ENP and MPI in the NA, and SST skill is best in N_SEAS5 except in the NA (Fig. 8a–c). HiFLOR-S, N_SPEAR, and ACE2_SPEAR share SPEAR-predicted SST, so no SST-skill differences among them are expected. In contrast, configurations show lower skill in predicting dynamical variables than thermodynamic variables in the WNP and ENP, but not in the NA. Skill relative to SPEAR is variable- and basin-dependent, though most configurations show lower skill than SPEAR for ζ_{850} in the ENP and V_s in the NA. In the ENP, SPEAR's ζ_{850} skill is significant (RCOR 0.42), but most other individual configurations show weaker, often non-significant skill, including the nine-model ensemble mean (RCOR 0.31).

In the NA, N_DWD's TCS skill is relatively lower than the other configurations (Fig. 4c), though its TGF climatology is not substantially different from theirs (Fig. 7m). N_DWD's large-scale-variable skill is instead lowest for thermodynamic variables and lower for dynamical variables (Fig. 8c), and its dominant TC-genesis driver differs entirely from observations in both the N1 and N2 sub-domains. These biases in the large-scale variables and in TC genesis's response to them are consistent with N_DWD's weakest basin-total TCS skill in the NA.

In the WNP, ACE2_SPEAR's skill in predicting TCS and ACE is the worst among the configurations (Fig. 4a,g). Although ACE2_SPEAR's thermodynamic-variable skill is comparable to

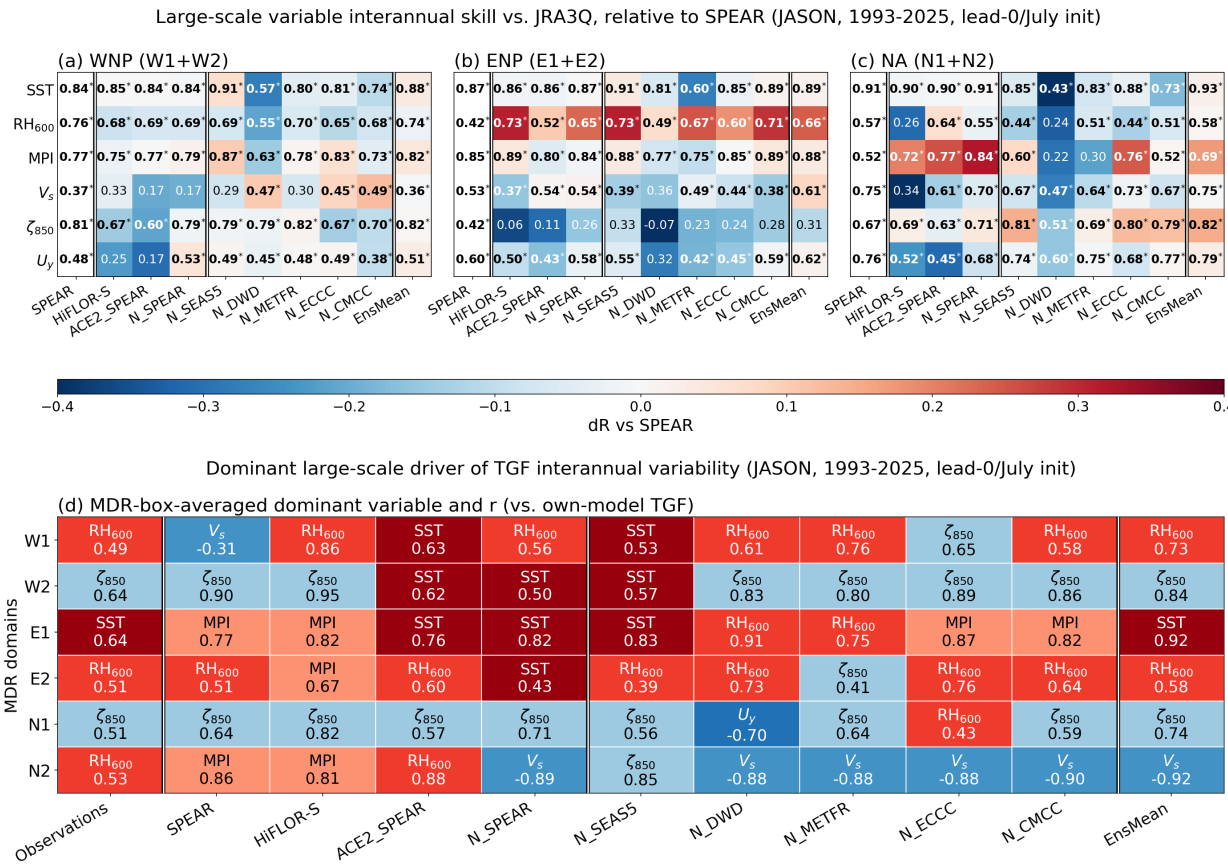

FIG. 8. Interannual skill and dominant driver of the large-scale TC-genesis environment, July–November (JASON), 1993–2025 (33 yr), July-initialized (0-month lead). (a–c) Skill of each configuration's area-averaged interannual series of six large-scale variables (rows; symbols described in Section 2f) against JRA-3Q reanalysis, for (a) WNP (union of sub-boxes W1+W2), (b) ENP (E1+E2), and (c) NA (N1+N2), relative to SPEAR. Columns give the nine hindcast configurations plus a multi-model ensemble (EnsMean). The number in each cell is that configuration's own RCOR against JRA-3Q; bold with an asterisk denotes significance at $p < 0.05$. Shading gives the difference in RCOR from SPEAR (red: exceeds SPEAR, blue: trails SPEAR); the SPEAR column has a white background. (d) For each of the six MDR sub-boxes (rows), the single large-scale variable with the highest-magnitude RCOR with that column's own area-averaged TGF (columns: observations, the nine hindcast configurations, and EnsMean), and that correlation coefficient; cell shading follows the same thermodynamic (red)/dynamical (blue) grouping as Fig. 7.

SPEAR's, its dynamical-variable skill is markedly lower (Fig. 8a). Moreover, in the W2 domain, ACE2_SPEAR critically underestimates TC genesis there (Fig. 7g). Also, the dominant driver for TC genesis in the W2 domain is a thermodynamic variable (SST) where observations and every other configuration identify a dynamical one (ζ_{850}, Fig. 8d). These underlying biases in TGF climatology, large-scale variables, and the response of TC genesis to those variables together cause the lowest skill in predicting TCS and ACE in the WNP. N_SPEAR and N_ECCC exceed SPEAR's TCS prediction skill (Fig. 4a). This could also partially be in line with the better spatial pattern of TGF climatology (Fig. 7i,q) as well as better sensitivity of TC genesis to large-scale variables, especially over W1, where N_SPEAR and N_ECCC show the highest dependence of W1 TGF on RH_{600}, as observed.

In the N2 sub-domain, observations identify RH_{600} as the strongest single correlate of interannual TGF (RCOR 0.53). SPEAR, HiFLOR-S, and ACE2_SPEAR agree that a thermodynamic variable dominates there (MPI or RH_{600}, RCOR 0.81–0.88), but all six NeuralGCM-based configurations instead identify a dynamical variable as dominant, predominantly V_s (RCOR −0.88 to −0.92, or ζ_{850} RCOR 0.85 for N_SEAS5)—a divide that follows model architecture rather than SST-forcing source. N_CMCC's higher TCS skill than SPEAR (Fig. 4c) may be partly coincidental: N_CMCC identifies a dynamical variable as the dominant driver of TC genesis in both N1 and N2—incorrectly, relative to observations—yet its skill in predicting that dynamical variable happens to exceed SPEAR's own (Fig. 8c). This illustrates that improved TCS skill in an AI-based configuration should not be taken at face value without examining whether the underlying TC-genesis-driver relationship is physically valid.

Overall, these diagnostics indicate that differences among the nine configurations are shaped by a complex combination of their skill in reproducing the climatological distribution of TC genesis and the extent to which their interannual TC-genesis variability is linked to large-scale drivers that are both skillfully predicted and physically consistent with observations. Moreover, as illustrated by N_CMCC, multiple biases within a configuration may interact nonlinearly and potentially compensate for one another, fortuitously yielding high TC prediction skill. However, the present correlational diagnostics are insufficient to determine whether differences in TC climatology and the large-scale environment fully explain the basin- and configuration-dependent TC-activity skill documented in Section 3b; further analysis is required. Nevertheless, these results are consistent with the principle established by Murakami et al. (2016b, 2025) that fidelity in the large-scale environment alone does not necessarily guarantee skillful TC-activity prediction.

4. Summary and discussion

This study asked whether AI weather–climate models—NeuralGCM (Kochkov et al. 2024) and ACE2 (Watt-Meyer et al. 2025)—can match or exceed the seasonal TC prediction skill of GFDL-SPEAR when forced by dynamically predicted, rather than persisted, SST and sea-ice boundary conditions. Across nine hindcast configurations evaluated over 1993–2025, the AI-based configurations were broadly competitive with the dynamical benchmark and, at the sub-basin scale, often superior to it, though their advantage was strongly basin-, metric-, and lead-dependent rather than uniform. In the NA basin, where Zhang et al. (2025)'s persistent-anomaly NeuralGCM configuration reported a TCS correlation of about 0.7 using a 20-member ensemble over 1990–2023, our dynamically-SST-forced configurations achieved comparable or higher skill (N_CMCC, a 50-member ensemble: RCOR 0.76; pooled multi-model mean: 0.72; versus SPEAR's 0.59). Given the differing ensemble sizes and verification periods, however, this comparison is only approximate. N_SPEAR further retained significant skill at 3–6-month leads where SPEAR's own skill had already decayed to non-significance, highlighting a practical benefit of forcing AI-based configurations with predicted rather than persisted SST at extended lead times. Model-specific limitations were equally clear: ACE2_SPEAR produced effectively no hurricane-intensity storms, and configurations sometimes achieved skill through a large-scale genesis-driver attribution that was internally consistent with model architecture but did not match the observed genesis-driver relationship, extending the principle of Murakami et al. (2016b, 2025) that environmental skill alone does not guarantee TC-activity skill.

Several limitations qualify these conclusions and point to priorities for future work. First, no persistent-anomaly control experiment was run; although the dynamically predicted SST framework is more physically motivated and extends evaluation to longer leads than Zhang et al. (2025)'s July-only configuration, its benefit relative to persisting the initialization anomaly remains unquantified and would require a matched pair of hindcasts to resolve. Second, the large-scale diagnostics are correlational, not causal; establishing causation would require targeted sensitivity experiments, such as forcing configurations with identical prescribed environments or perturbing individual boundary conditions. Third, the 33-yr record is short and the RCOR differences among top-performing configurations are small (0.05–0.15), so configuration rankings should be treated as indicative rather than definitive; longer records or additional initialization months would make them more robust. Fourth, the AI-based models' TC detection thresholds were calibrated empirically rather than derived from physical criteria, introducing some sensitivity to that choice. Fifth, ACE2's inability to generate hurricane-intensity storms precludes intensity-dependent evaluation and points to warm-core representation as a priority for improving data-driven emulators. Sixth, NeuralGCM forecasts initialized in January and February were unavailable because of unresolved computational instability, limiting the accessible lead range and the ability to test N_SPEAR's extended-lead advantage at 5–6 months. Seventh, the boundary conditions prescribed here are SPEAR's full predicted fields rather than an anomaly-forcing approach (adding the predicted anomaly to observed climatology), which was not tested here but could yield more stable integrations and higher skill. Finally, all AI-based configurations used a single pre-trained deterministic model with prescribed SST and no air–sea coupling; stochastic variants, higher resolution, and coupled frameworks remain unexplored. A further benchmark, beyond the scope of this study, would be to drive all four models with observed SST and sea ice, separating limitations from boundary-condition uncertainty from those intrinsic to each configuration's representation of the atmosphere and TC genesis.

For operational seasonal TC forecasting, these results suggest that AI weather–climate configurations forced by dynamically predicted SST are already competitive with an established dynamical model at a small fraction of its computational cost, highlighting the potential for prediction frameworks that integrate the strengths of AI and dynamical modeling. More broadly, combining a diverse set of configurations—spanning a coupled dynamical model and multiple structurally distinct, computationally inexpensive AI-based configurations—facilitates cross-model comparison that can help pinpoint the sources of configuration biases. Such a multi-model approach is also valuable for representing forecast uncertainty, since pooling structurally diverse configurations captures a wider range of possible outcomes than any single configuration's own ensemble alone. At the same time, these results underscore that skill scores alone are an insufficient basis for adopting a new prediction configuration operationally; understanding whether a configuration's TC-genesis response to the large-scale environment is physically consistent, rather than a fortuitous compensating bias, should inform which configurations are trusted for real-time seasonal outlooks.

Acknowledgments. We acknowledge ECMWF and the Copernicus Climate Change Service for providing the C3S seasonal forecast data, the Japan Meteorological Agency for JRA-3Q, the Allen

Institute for Artificial Intelligence for ACE2, and Google for NeuralGCM. The authors thank Dr. Spencer K. Clark and Dr. Jan-Huey Chen for their suggestions and comments. The authors declare no competing financial interests. The statements, findings, and conclusions are those of the authors and do not necessarily reflect the views of the National Oceanic and Atmospheric Administration or the U.S. Department of Commerce. During manuscript preparation, the authors used Claude Code (Anthropic), a generative AI tool, to assist with English-language grammar and spelling proofreading; the authors reviewed and edited all output and take full responsibility for the content of this publication.

Data availability statement. The observed TC best-track data used in this study are from the International Best Track Archive for Climate Stewardship (IBTrACS) Project, Version 4r01 (Knapp et al. 2010; Gahtan et al. 2024), distributed by NOAA's National Centers for Environmental Information at `https://doi.org/10.25921/82ty-9e16`. The large-scale environmental variables were derived from the Japanese Reanalysis for Three Quarters of a Century (JRA-3Q; Kosaka et al. 2024), available from the NSF NCAR Geoscience Data Exchange (dataset d640000) at `https://doi.org/10.5065/AVTZ-1H78` under a CC BY-NC-SA 4.0 license. The predicted SST and sea-ice fields prescribed in the N_SEAS5, N_DWD, N_METFR, N_ECCC, and N_CMCC experiments were obtained from the Copernicus Climate Change Service (C3S) Climate Data Store dataset "Seasonal forecast daily and subdaily data on single levels," available at `https://doi.org/10.24381/cds.181d637e` under a CC BY license. GFDL-SPEAR seasonal forecasts, which provide the boundary conditions for the HiFLOR-S, ACE2_SPEAR, and N_SPEAR experiments, are distributed through the North American Multi-Model Ensemble (NMME; Kirtman et al. 2014) at `https://www.cpc.ncep.noaa.gov/products/NMME/`. The SPEAR and HiFLOR-S hindcast output analyzed here is available from the corresponding author upon reasonable request. The pre-trained ACE2-ERA5 configuration checkpoint is available from the Allen Institute for AI at `https://huggingface.co/allenai/ACE2-ERA5`, and the associated training, inference, and evaluation code at `https://github.com/ai2cm/ace` (Watt-Meyer et al. 2025). The NeuralGCM code base (Kochkov et al. 2024) is available at `https://github.com/neuralgcm/neuralgcm` (`https://doi.org/10.5281/zenodo.14715068`) under an Apache License 2.0. The pre-trained checkpoints, including the 1.4° deterministic model used here, are distributed by Google at `gs://neuralgcm/configurations/` under a CC BY-SA 4.0 license. TCs were detected from configuration output using the GFDL QuickTracks algorithm (Harris et al. 2016; Murakami et al. 2015), available at `https://github.com/lharris4/GFDL_quick_tracks`. The analysis and figure-generation scripts supporting the findings of this study are available from the corresponding author upon reasonable request.

References

Adcroft, A., and Coauthors, 2019: The GFDL global ocean and sea ice model OM4.0: Model description and simulation features. *J. Adv. Model. Earth Syst.*, **11**, 3167–3211, https://doi.org/10.1029/2019MS001726.

Bell, G. D., and Coauthors, 2000: The 1999 North Atlantic and Eastern North Pacific hurricane season. *Bull. Amer. Meteor. Soc.*, **81**, S19–S22, https://doi.org/10.1175/1520-0477(2000)081⟨1328:CAF⟩2.3.CO;2.

Bi, K., L. Xie, H. Zhang, X. Chen, X. Gu, and Q. Tian, 2023: Accurate medium-range global weather forecasting with 3D neural networks. *Nature*, **619**, 533–538, https://doi.org/10.1038/s41586-023-06185-3.

Bister, M., and K. A. Emanuel, 1998: Dissipative heating and hurricane intensity. *Meteor. Atmos. Phys.*, **52**, 233–240, https://doi.org/10.1007/BF01030791.

Brenowitz, N. D., and C. S. Bretherton, 2019: Spatially extended tests of a neural network parametrization trained by coarse-graining. *J. Adv. Model. Earth Syst.*, **11**, 2728–2744, https://doi.org/10.1029/2019MS001711.

Bretherton, C. S., M. Widmann, V. P. Dymnikov, J. M. Wallace, and I. Bladé, 1999: The effective number of spatial degrees of freedom of a time-varying field. *J. Climate*, **12**, 1990–2009, https://doi.org/10.1175/1520-0442(1999)012⟨1990:TENOSD⟩2.0.CO;2.

Camargo, S. J., A. G. Barnston, P. J. Klotzbach, and C. W. Landsea, 2007: Seasonal tropical cyclone forecasts. *WMO Bull.*, **56**, 297–307.

Chu, P.-S., and H. Murakami, 2022: *Climate Variability and Tropical Cyclone Activity*. Cambridge University Press, https://doi.org/10.1017/9781108586467.

Chu, P.-S., and X. Zhao, 2007: A Bayesian regression approach for predicting seasonal tropical cyclone activity over the Central North Pacific. *J. Climate*, **20**, 4002–4013, https://doi.org/10.1175/JCLI4214.1.

Chu, W., J. L. García-Franco, S. J. Camargo, C.-Y. Lee, M. K. Tippett, H. Murakami, J. W. Baldwin, and S. Frucht, 2026: Historical and projected tropical cyclone characteristics in SPEAR large ensemble simulations. *Earth's Future*, **14**, e2025EF007 720, https://doi.org/10.1029/2025EF007720.

Comaniciu, A., and H. Murakami, 2026: A novel method for improving seasonal Atlantic hurricane activity prediction based on convolutional neural networks and visualization maps. *Artif. Intell. Earth Syst.*, **5**, 250 010, https://doi.org/10.1175/AIES-D-25-0010.1.

Delworth, T. L., and Coauthors, 2006: GFDL's CM2 global coupled climate models. part I: Formulation and simulation characteristics. *J. Climate*, **19**, 643–674, https://doi.org/10.1175/JCLI3629.1.

Delworth, T. L., and Coauthors, 2020: SPEAR: The next generation GFDL modeling system for seasonal to multidecadal prediction and projection. *J. Adv. Model. Earth Syst.*, **12**, e2019MS001 895, https://doi.org/10.1029/2019MS001895.

Duan, W., and C. Wei, 2013: The "spring predictability barrier" for ENSO predictions and its possible mechanism: results from a fully coupled model. *Int. J. Climatol.*, **33**, 1280–1292, https://doi.org/10.1002/joc.3513.

Emanuel, K. A., and D. S. Nolan, 2004: Tropical cyclone activity and global climate. *Preprints, 26th Conf. on Hurricanes and Tropical Meteorology*, Amer. Meteor. Soc., Miami, FL, 240–241.

Fu, D., P. Chang, and X. Liu, 2023: Using convolutional neural network to emulate seasonal tropical cyclone activity. *J. Adv. Model. Earth Syst.*, **15**, e2022MS003 596, https://doi.org/10.1029/2022MS003596.

Gahtan, J., K. R. Knapp, C. J. Schreck, III, H. J. Diamond, J. P. Kossin, and M. C. Kruk, 2024: International best track archive for climate stewardship (IBTrACS) project, version 4r01. NOAA National Centers for Environmental Information, https://doi.org/10.25921/82ty-9e16.

Gray, W. M., 1979: Hurricanes: Their formation, structure and likely role in the tropical circulation. *Meteorology over the Tropical Oceans*, D. B. Shaw, Ed., Royal Meteorological Society, 155–218.

Harris, L. M., S.-J. Lin, and C. Tu, 2016: High-resolution climate simulations using GFDL HiRAM with a stretched global grid. *J. Climate*, **29**, 4293–4314, https://doi.org/10.1175/JCLI-D-15-0389.1.

Henn, B., and Coauthors, 2026: AIMIP phase 1: Systematic evaluations of AI weather and climate models. arXiv, arXiv:2605.06944, https://doi.org/10.48550/arXiv.2605.06944.

Hersbach, H., and Coauthors, 2020: The ERA5 global reanalysis. *Quart. J. Roy. Meteor. Soc.*, **146**, 1999–2049, https://doi.org/10.1002/qj.3803.

Kent, C., A. A. Scaife, N. J. Dunstone, D. Smith, S. C. Hardiman, T. Dunstan, and O. Watt-Meyer, 2025: Skilful global seasonal predictions from a machine learning weather model trained on reanalysis data. *npj Clim. Atmos. Sci.*, **8**, 314, https://doi.org/10.1038/s41612-025-01198-3.

Kim, H.-S., C.-H. Ho, J.-H. Kim, and P.-S. Chu, 2012: Track-pattern-based model for seasonal prediction of tropical cyclone activity in the Western North Pacific. *J. Climate*, **25**, 4660–4678, https://doi.org/10.1175/JCLI-D-11-00236.1.

Kirtman, B. P., and Coauthors, 2014: The North American multimodel ensemble: Phase-1 seasonal-to-interannual prediction; phase-2 toward developing intraseasonal prediction. *Bull. Amer. Meteor. Soc.*, **95**, 585–601, https://doi.org/10.1175/BAMS-D-12-00050.1.

Knapp, K. R., M. C. Kruk, D. H. Levinson, H. J. Diamond, and C. J. Neumann, 2010: The international best track archive for climate stewardship (IBTrACS): Unifying tropical cyclone best track data. *Bull. Amer. Meteor. Soc.*, **91**, 363–376, https://doi.org/10.1175/2009BAMS2755.1.

Kochkov, D., and Coauthors, 2024: Neural general circulation models for weather and climate. *Nature*, **632**, 1060–1066, https://doi.org/10.1038/s41586-024-07744-y.

Kosaka, Y., and Coauthors, 2024: The JRA-3Q reanalysis. *J. Meteor. Soc. Japan*, **102**, 49–109, https://doi.org/10.2151/jmsj.2024-004.

Krichene, H., T. Vogt, F. Piontek, T. Geiger, C. Schötz, and C. Otto, 2023: The social costs of tropical cyclones. *Nat. Commun.*, **14**, 7294, https://doi.org/10.1038/s41467-023-43114-4.

Lam, R., and Coauthors, 2023: Learning skillful medium-range global weather forecasting. *Science*, **382**, 1416–1421, https://doi.org/10.1126/science.adi2336.

Lemoine, D., and S. Kapnick, 2024: Financial markets value skillful forecasts of seasonal climate. *Nat. Commun.*, **15**, 4059, https://doi.org/10.1038/s41467-024-48420-z.

Li, X., S. Yang, H. Wang, X. Jia, and A. Kumar, 2013: A dynamical-statistical forecast model for the annual frequency of Western Pacific tropical cyclones based on the NCEP climate forecast system version 2. *J. Geophys. Res.*, **118**, 12,061–12,074, https://doi.org/10.1002/2013JD020708.

Lu, F., and Coauthors, 2020: GFDL's SPEAR seasonal prediction system: Initialization and ocean tendency adjustment (OTA) for coupled model predictions. *J. Adv. Model. Earth Syst.*, **12**, e2020MS002 149, https://doi.org/10.1029/2020MS002149.

Murakami, H., and P.-S. Chu, 2025: Forecasting the impacts associated with tropical cyclones. *Tropical Cyclones and Associated Impacts*, Elsevier, 189–221, https://doi.org/10.1016/B978-0-323-95390-0.00010-8.

Murakami, H., T. L. Delworth, W. F. Cooke, M. Zhao, B. Xiang, and P.-C. Hsu, 2020: Detected climatic change in global distribution of tropical cyclones. *Proc. Natl. Acad. Sci. (USA)*, **117**, 10 706–10 714, https://doi.org/10.1073/pnas.1922500117.

Murakami, H., T. L. Delworth, N. C. Johnson, F. Lu, C. E. McHugh, and L. Jia, 2025: Seasonal forecasts of tropical cyclones using GFDL SPEAR and HiFLOR-S. *J. Climate*, **38**, 2015–2030, https://doi.org/10.1175/JCLI-D-24-0356.1.

Murakami, H., G. Villarini, G. A. Vecchi, W. Zhang, and R. Gudgel, 2016a: Statistical–dynamical seasonal forecast of North Atlantic and U.S. landfalling tropical cyclones using the high-resolution GFDL FLOR coupled model. *Mon. Wea. Rev.*, **144**, 2101–2123, https://doi.org/10.1175/MWR-D-15-0308.1.

Murakami, H., and B. Wang, 2022: Patterns and frequency of projected future tropical cyclone genesis are governed by dynamic effects. *Commun. Earth Environ.*, **3**, 77, https://doi.org/10.1038/s43247-022-00410-z.

Murakami, H., and Coauthors, 2015: Simulation and prediction of Category 4 and 5 hurricanes in the high-resolution GFDL HiFLOR coupled climate model. *J. Climate*, **28**, 9058–9079, https://doi.org/10.1175/JCLI-D-15-0216.1.

Murakami, H., and Coauthors, 2016b: Seasonal forecasts of major hurricanes and landfalling tropical cyclones using a high-resolution GFDL coupled climate model. *J. Climate*, **29**, 7977–7989, https://doi.org/10.1175/JCLI-D-16-0233.1.

Siddik, M. A., and A. R. M. T. Islam, 2024: A systematic review of cyclonic disaster: Damage-loss, consequences, adaptation strategies, and future scopes. *Heliyon*, **10**, e33 345, https://doi.org/10.1016/j.heliyon.2024.e33345.

Takaya, Y., and Coauthors, 2023: Recent advances in seasonal and multi-annual tropical cyclone forecasting. *Trop. Cyclone Res. Rev.*, **12**, 182–199, https://doi.org/10.1016/j.tcrr.2023.09.003.

Tang, B., and K. Emanuel, 2012: A ventilation index for tropical cyclones. *Bull. Amer. Meteor. Soc.*, **93 (12)**, 1901–1912, https://doi.org/10.1175/BAMS-D-11-00165.1.

Tippett, M. K., S. J. Camargo, and A. H. Sobel, 2011: A poisson regression index for tropical cyclone genesis and the role of large-scale vorticity in genesis. *J. Climate*, **24 (9)**, 2335–2357, https://doi.org/10.1175/2010JCLI3811.1.

Vecchi, G. A., M. Zhao, H. Wang, G. Villarini, A. Rosati, A. Kumar, I. M. Held, and R. Gudgel, 2011: Statistical–dynamical predictions of seasonal North Atlantic hurricane activity. *Mon. Wea. Rev.*, **139**, 1070–1082, https://doi.org/10.1175/2010MWR3499.1.

Vecchi, G. A., and Coauthors, 2014: On the seasonal forecasting of regional tropical cyclone activity. *J. Climate*, **27**, 7994–8016, https://doi.org/10.1175/JCLI-D-14-00158.1.

Vitart, F., and T. N. Stockdale, 2001: Seasonal forecasting of tropical storms using coupled GCM integrations. *Mon. Wea. Rev.*, **129**, 2521–2537, https://doi.org/10.1175/1520-0493(2001)129⟨2521:SFOTSU⟩2.0.CO;2.

Wang, B., and H. Murakami, 2020: Dynamic genesis potential index for diagnosing present-day and future global tropical cyclone genesis. *Environ. Res. Lett.*, **15**, 114 008, https://doi.org/10.1088/1748-9326/abbb01.

Watt-Meyer, O., and Coauthors, 2024: Neural network parameterization of subgrid-scale physics from a realistic geography global storm-resolving simulation. *J. Adv. Model. Earth Syst.*, **16**, e2023MS003 668, https://doi.org/10.1029/2023MS003668.

Watt-Meyer, O., and Coauthors, 2025: ACE2: accurately learning subseasonal to decadal atmospheric variability and forced responses. *npj Clim. Atmos. Sci.*, **8**, 205, https://doi.org/10.1038/s41612-025-01090-0.

Yuval, J., P. A. O'Gorman, and C. N. Hill, 2021: Use of neural networks for stable, accurate and physically consistent parameterization of subgrid atmospheric processes with good performance at reduced precision. *Geophys. Res. Lett.*, **48**, e2020GL091 363, https://doi.org/10.1029/2020GL091363.

Zhang, G., M. Rao, J. Yuval, and M. Zhao, 2025: Advancing seasonal prediction of tropical cyclone activity with a hybrid AI-physics climate model. *Environ. Res. Lett.*, **20**, 094 031, https://doi.org/10.1088/1748-9326/adf864.

Zhang, W., G. A. Vecchi, G. Villarini, H. Murakami, T. Delworth, L. Jia, R. Gudgel, and F. Zeng, 2016: Simulated connections between ENSO and tropical cyclones near Guam in a high-resolution GFDL coupled climate model: Implications for seasonal forecasting. *J. Climate*, **29**, 8231–8248, https://doi.org/10.1175/JCLI-D-16-0126.1.

Zhang, W., G. A. Vecchi, G. Villarini, H. Murakami, R. Gudgel, and X. Yang, 2017a: Statistical–dynamical seasonal forecast of Western North Pacific and East Asia landfalling tropical cyclones using the GFDL FLOR coupled climate model. *J. Climate*, **30**, 2209–2232, https://doi.org/10.1175/JCLI-D-16-0487.1.

Zhang, X., S. Zhong, Z. Wu, and Y. Li, 2017b: Seasonal prediction of the typhoon genesis frequency over the Western North Pacific with a Poisson regression model. *Climate Dyn.*, **51**, 4585–4600, https://doi.org/10.1007/s00382-017-3654-5.

Zhao, M., and Coauthors, 2018: The GFDL global atmosphere and land model AM4.0/LM4.0: 2. model description, sensitivity studies, and tuning strategies. *J. Adv. Model. Earth Syst.*, **10**, 735–769, https://doi.org/10.1002/2017MS001209.

Supplemental Material for
"Skillful Seasonal Tropical Cyclone Prediction with AI Weather–Climate Models Forced by Dynamically Predicted SSTs"

Hiroyuki Murakami[a] and Baoqiang Xiang[a,b]

[a] *National Oceanic and Atmospheric Administration/Geophysical Fluid Dynamics Laboratory, Princeton, New Jersey, USA*

[b] *University Corporation for Atmospheric Research, Boulder, CO, USA*

Submitted to the *Journal of Climate* on September 21, 2026

Corresponding author: Hiroyuki Murakami, NOAA/GFDL, 201 Forrestal Rd., Princeton, NJ 08540-6649. E-mail: hir.murakami@gmail.com

ABSTRACT: This document contains supplemental material for the main manuscript. The Supplementary Results section provides a detailed description of the ensemble-pooling analysis. The remainder of this document consists of Supplementary Figures cited in the main text or elsewhere in this document.

S1. Supplementary Results

Would a skill-based subset outperform the full multi-model ensemble?

The multi-model ensemble, shown in Figs. 3j and 4, pools every member from all nine configurations with equal weight, regardless of each configuration's individual skill. This raises a natural question: would selecting or upweighting only the most skillful configurations yield a more skillful pooled forecast than uniform pooling of all nine configurations? Using the same 33-yr record both to identify the most skillful configuration and to evaluate the performance of such a skill-based selection strategy could lead to an overestimation of forecast skill due to selection bias. This concern is particularly relevant given the limited sample size—only 33 years (effectively n_{eff} ≈28–33 after the autocorrelation adjustment of Section 2c)—and the relatively small RCOR differences among the top-performing configurations (typically 0.05–0.15). These small margins make the apparent ranking sensitive to sampling variability. We therefore evaluate this question with leave-one-year-out (LOYO) cross-validation. For each of the 33 hindcast years in turn, that year is withheld, and the nine configurations are ranked by their 32-yr RCOR against observations computed from the remaining years. The withheld year's forecast is then formed by pooling the ensemble members of only the top-K-ranked configurations, for $K = 1$ (single best configuration) through $K = 9$ (all configurations, equivalent to Fig. 3j). Repeating this over all 33 folds yields a genuinely out-of-sample RCOR and MSSS for every candidate K.

Before interpreting the $K = 1$ curve as "the best configuration's own skill," we first check whether the training-fold top-K set is even a stable, well-defined quantity, since a ranking based on a 0.05–0.15 RCOR margin could plausibly flip from fold to fold. Figure S9 shows, for TCS at WNP (a), ENP (b), and NA (c), each configuration's share of the $K \times 33$ top-K "slots" filled across the 33 folds, for $K = 1$, 3, and 5 and for both the June and July initializations. At $K = 1$, a single configuration dominates the top rank in four of the six (basin, initialization) combinations: N_SPEAR (31/33 folds, 94%) for WNP–July, N_ECCC (33/33, 100%) for WNP–June, N_METFR (29/33, 88%) for ENP–July, and N_CMCC (33/33, 100%) for NA–July. In these cases the training-fold "best configuration" is a stable, well-defined choice, and its $K = 1$ out-of-sample skill (discussed below) approximates that one configuration's genuine skill rather than an artifact of which year happened to be withheld. The remaining two combinations are less stable at $K = 1$. NA–June is led by

SPEAR but only in 28/33 (85%) folds, with three other configurations splitting the rest. ENP–June splits between N_CMCC (18/33, 55%) and N_ECCC (11/33, 33%), with N_SEAS5 taking the remaining 4/33 (12%).

This instability at $K = 1$ is substantially reduced once a few more configurations are pooled. For ENP–June, whose top rank was the most fragmented of the six cases, the top-5 set at $K = 5$ is occupied almost entirely by five configurations in near-equal, near-100%-of-folds shares (N_ECCC, HiFLOR-S, N_SEAS5, and N_CMCC each ≈20%, N_METFR ≈19%). The same five configurations are selected in virtually every fold, even though which one of them ranks #1 varies. ENP–July shows the clearest case of this convergence already at $K = 3$, where N_CMCC, N_METFR, and N_SEAS5 each occupy exactly 33.3% of the top-3 slots; that is, these three configurations are the top-3-ranked set in literally every one of the 33 folds. In both cases, the near-equal partitioning of slots among the members of an otherwise stable top set—rather than one configuration dominating it—indicates that these leading configurations have statistically indistinguishable skill. Which one attains the highest rank in a given fold is essentially sampling noise, even though membership in the top set itself is robust.

Figure S10 shows the resulting out-of-sample RCOR (a,c) and MSSS (b,d) as a function of K for TCS, separately for the July (a,b) and June (c,d) initializations, at NA, WNP, and ENP. Four points emerge. First, skill is systematically higher for the July than the June initialization at NA and ENP (e.g., ENP MSSS at $K = 3$: 0.67 for July vs. 0.47 for June), consistent with the shorter lead carrying more up-to-date information. WNP shows comparatively little sensitivity to the one-month lead difference (MSSS at $K = 9$: 0.18 July vs. 0.19 June). Second, ENP has the highest MSSS of the three basins at both initialization months, while WNP has the lowest, a ranking that holds regardless of lead time. Third, skill at low K (1–3) is noticeably less stable than at higher K, most visibly for ENP–June RCOR (Fig. S10c), which rises from 0.34 at $K = 1$ to 0.64 at $K = 3$. This is consistent with the fold-to-fold selection instability documented in Fig. S9 for that same (basin, initialization) pair. Fourth, for most basin/initialization combinations skill changes little beyond $K \approx 5$, matching the top-K-set convergence seen directly in Fig. S9. By $K = 5$ the same handful of configurations are selected in nearly every fold, so pooling at least about five configurations gives skill close to whatever the eventual $K = 9$ value is, without requiring confident identification of a single best configuration. Finally, comparing each $K = 1$–8 against $K = 9$ directly answers the opening question: no single K is uniformly best. For RCOR, five of the six (basin, initialization) cases have at least one $K < 9$ exceeding $K = 9$, sometimes substantially (ENP–July: 0.77 at $K = 3$ vs. 0.71 at $K = 9$; WNP–June: 0.51 at $K = 1$ vs. 0.43 at $K = 9$). Only NA–June is best at $K = 9$. MSSS is more mixed: NA–June and ENP–June are best at $K = 9$, whereas WNP–July, WNP–June, and especially ENP–July (0.67 at $K = 3$ vs. 0.62 at $K = 9$) are better at some smaller K. Because which K performs best varies unpredictably by basin and initialization month, selecting a smaller skill-based subset is not a reliably better strategy than uniform pooling of all nine configurations. It is sometimes better, sometimes worse, and which outcome occurs cannot be anticipated in advance, at least in this study.

S2. Supplementary Figures

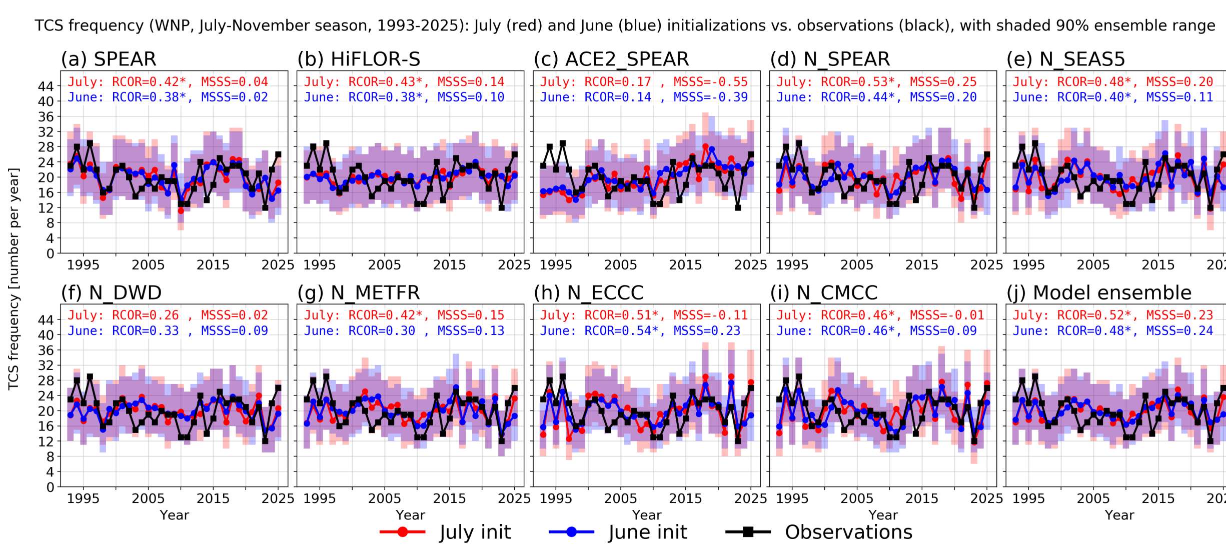

Fig. S1. As in Fig. 3, but for WNP.

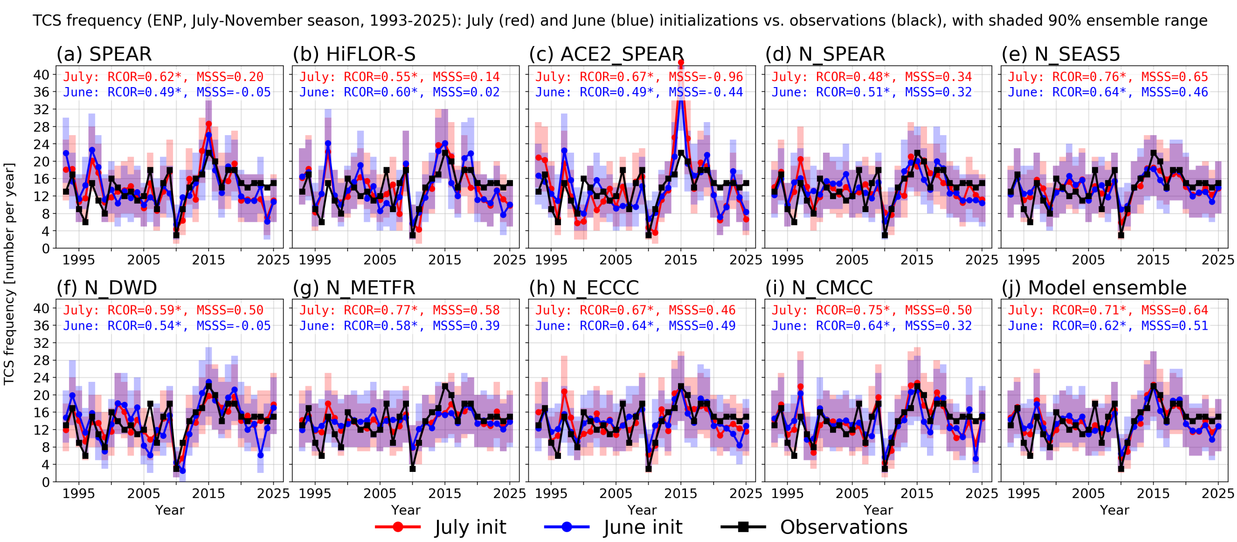

FIG. S2. As in Fig. 3, but for ENP.

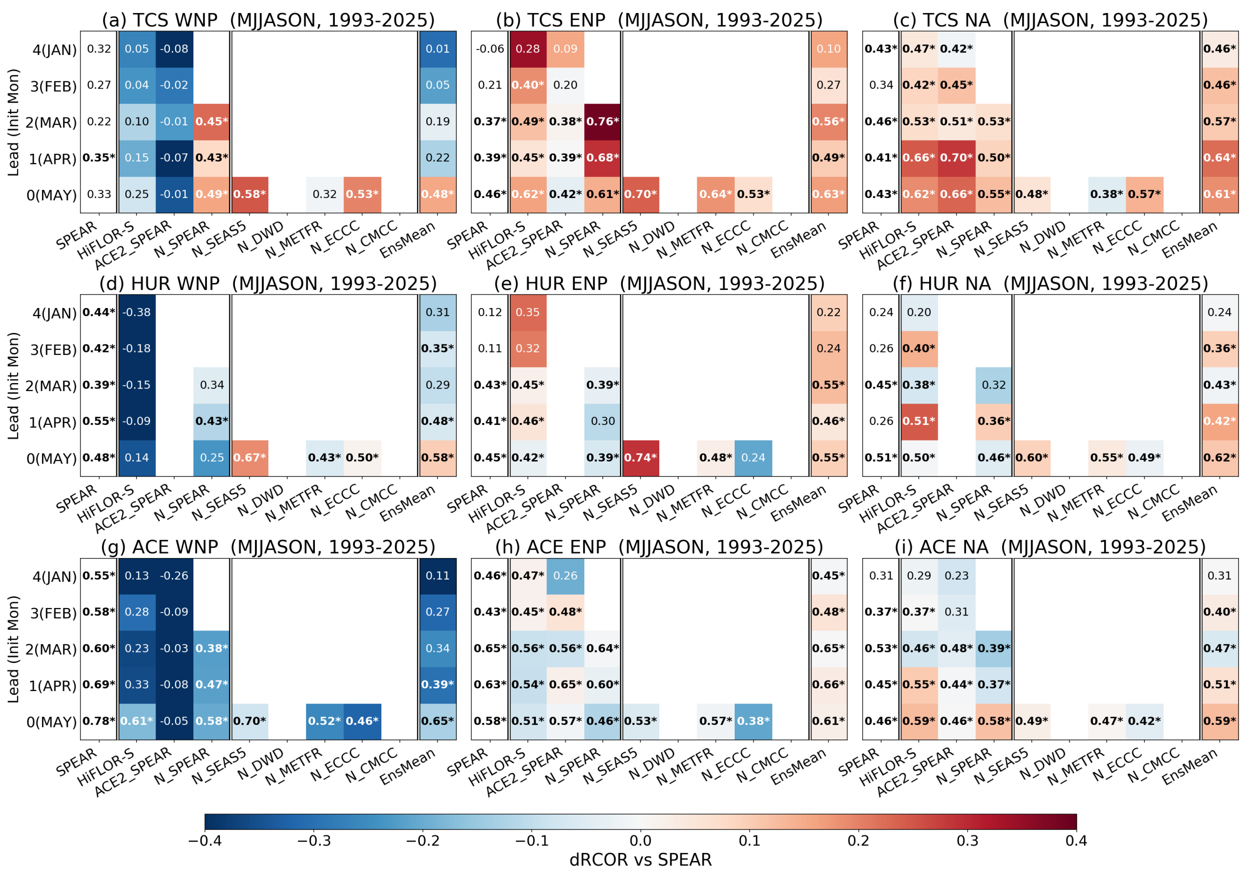

FIG. S3. As in Fig. 4, but for May–November forecasts.

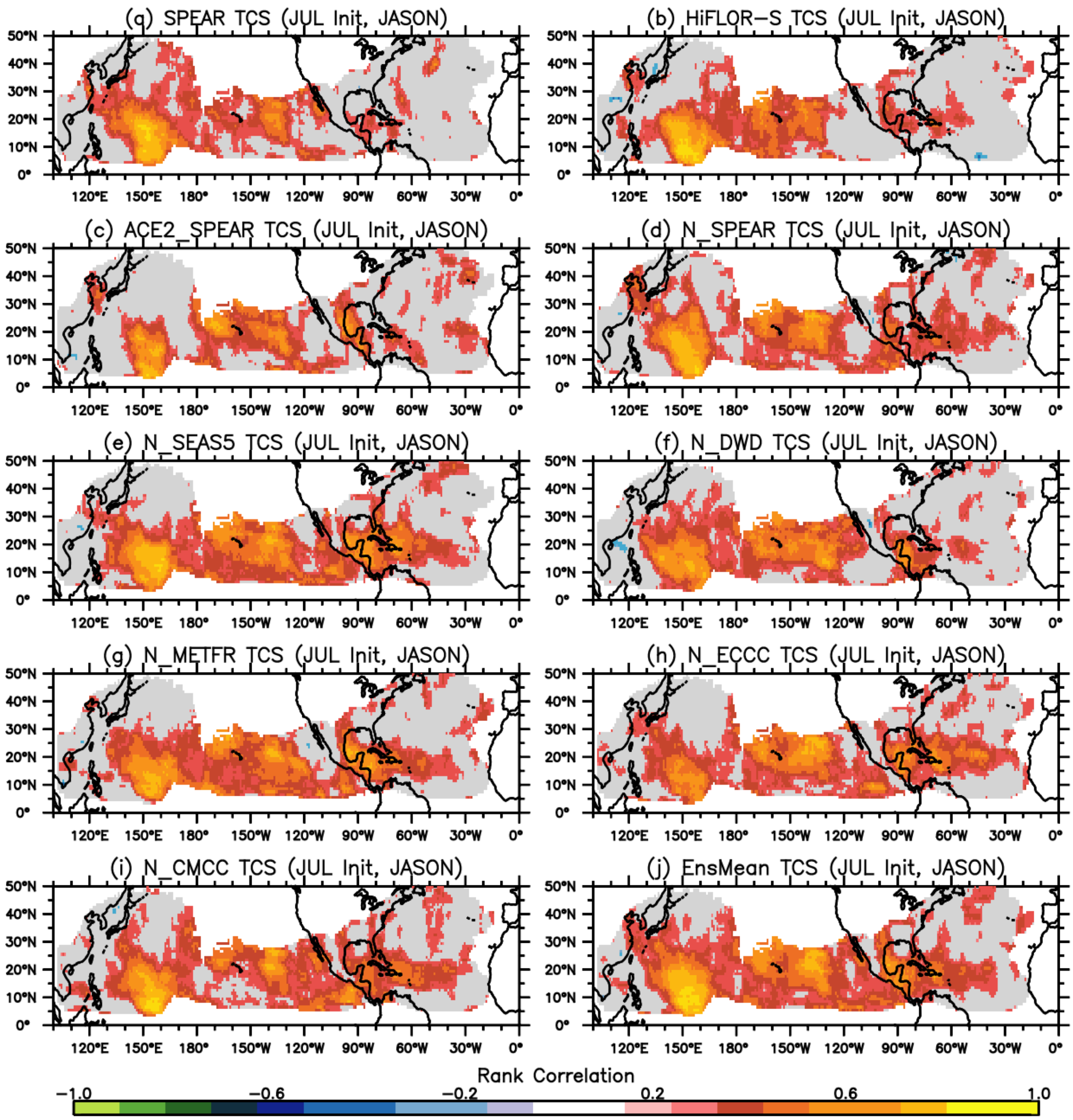

FIG. S4. As in Fig. 5, but for HUR.

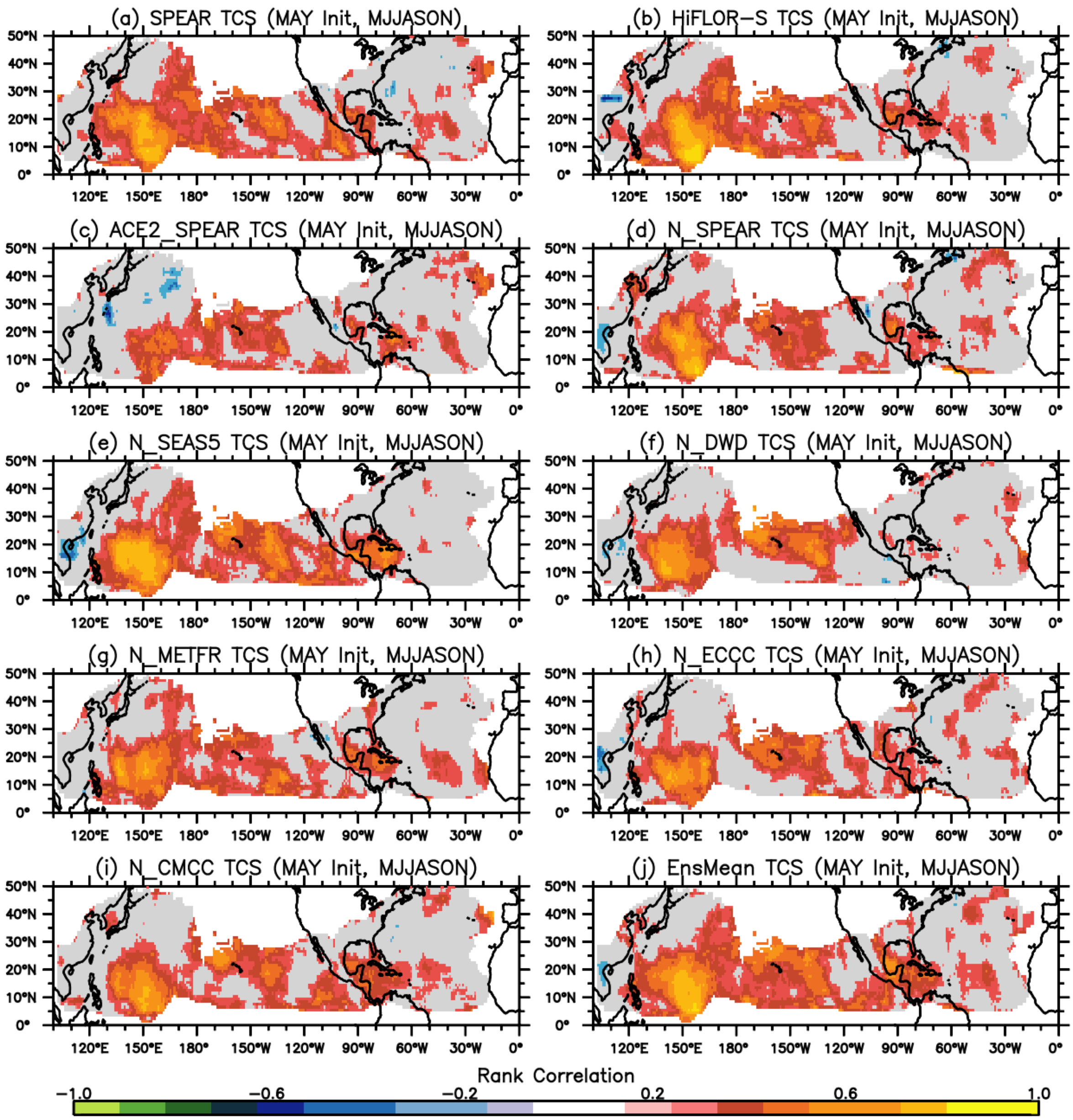

FIG. S5. As in Fig. 5, but for the May–November forecasts from the May initializations.

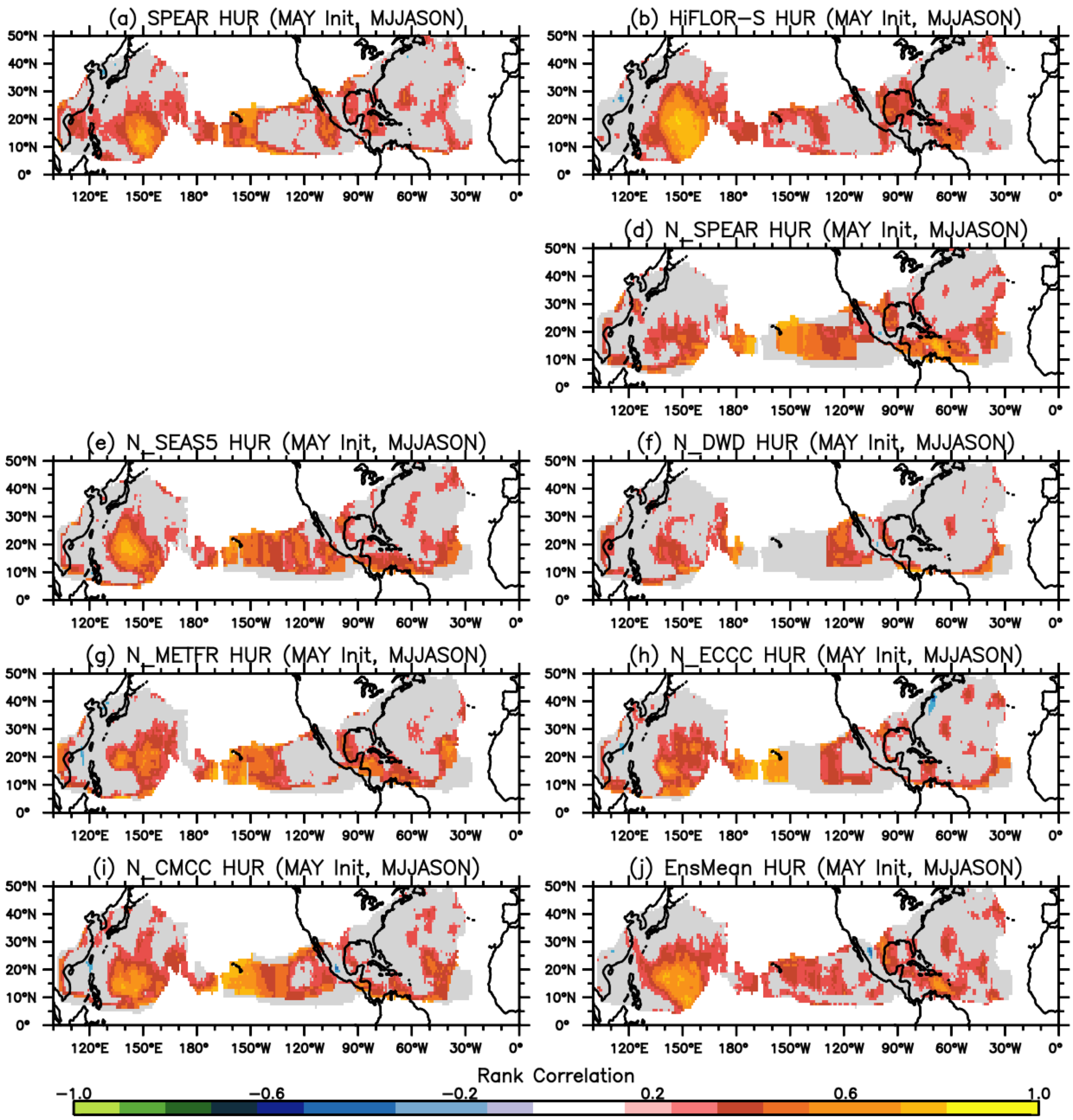

Fig. S6. As in Fig. 5, but for HUR for the May–November forecasts from the May initializations.

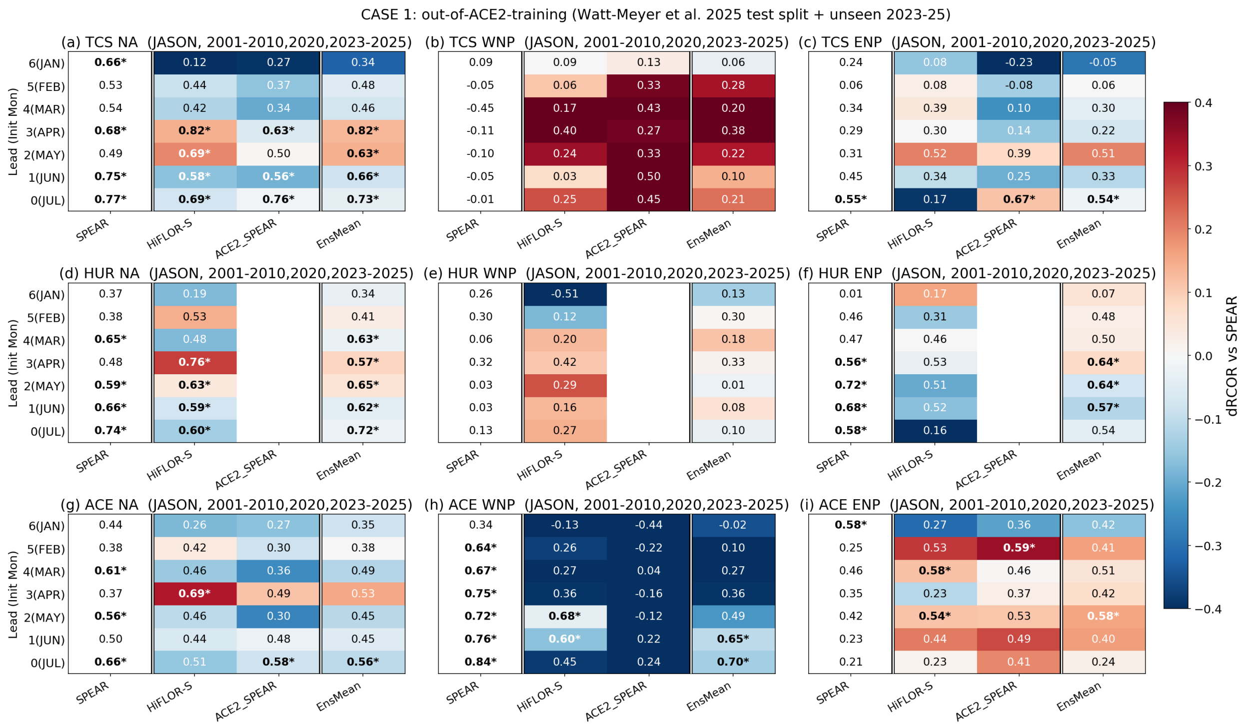

Fig. S7. Out-of-training-sample robustness check for ACE2_SPEAR. As in the main-text correlation-skill comparison (Spearman rank correlation, RCOR, between predicted and observed basin-total seasonal (July–November, JASON) tropical storm frequency (TCS; a–c), hurricane frequency (HUR; d–f), and accumulated cyclone energy (ACE; g–i) for lead times of 0–6 months over NA, WNP, and ENP), but verification is restricted to the 14 years falling outside both ACE2's own ERA5 training split (1940–1995, 2011–2019, 2021–2022) and its validation split (1996–2000; Watt-Meyer et al. 2025): 2001–2010, 2020, and 2023–2025. Only the three configurations with a common 12-month forecast length over the full record are shown—SPEAR, HiFLOR-S, and ACE2_SPEAR—plus their equal-weighted mean (EnsMean); shading gives the difference in RCOR from SPEAR (ΔRCOR), and bold with an asterisk denotes RCOR significant at $p < 0.05$ using the autocorrelation-adjusted two-tailed test described in the main text (Section 2; Bretherton et al. 1999), with the lag-1 autocorrelation estimated separately within the 2001–2010, 2020, and 2023–2025 blocks and combined, since the three blocks are not temporally adjacent. HUR panels omit ACE2_SPEAR, which produces effectively no hurricane-intensity storms at any period (main text Results, subsection a). Relative to the full-period comparison (Fig. 4), 63% of cells retain the same sign of ΔRCOR; reversals large enough to plausibly alter a qualitative conclusion ($|\Delta\text{RCOR}| \geq 0.10$ in both periods) occur in 15% of cells, of which 13 of 16 favor ACE2_SPEAR, concentrated in WNP TCS at leads where SPEAR's own out-of-sample correlation weakens (e.g., March initialization: RCOR −0.45 here versus +0.27 over the full period). This shift is consistent with sampling variability in SPEAR's smaller, non-contiguous out-of-sample estimate rather than a genuine change in ACE2_SPEAR's skill, and does not support training-sample overlap as an explanation for ACE2_SPEAR's competitiveness with SPEAR.

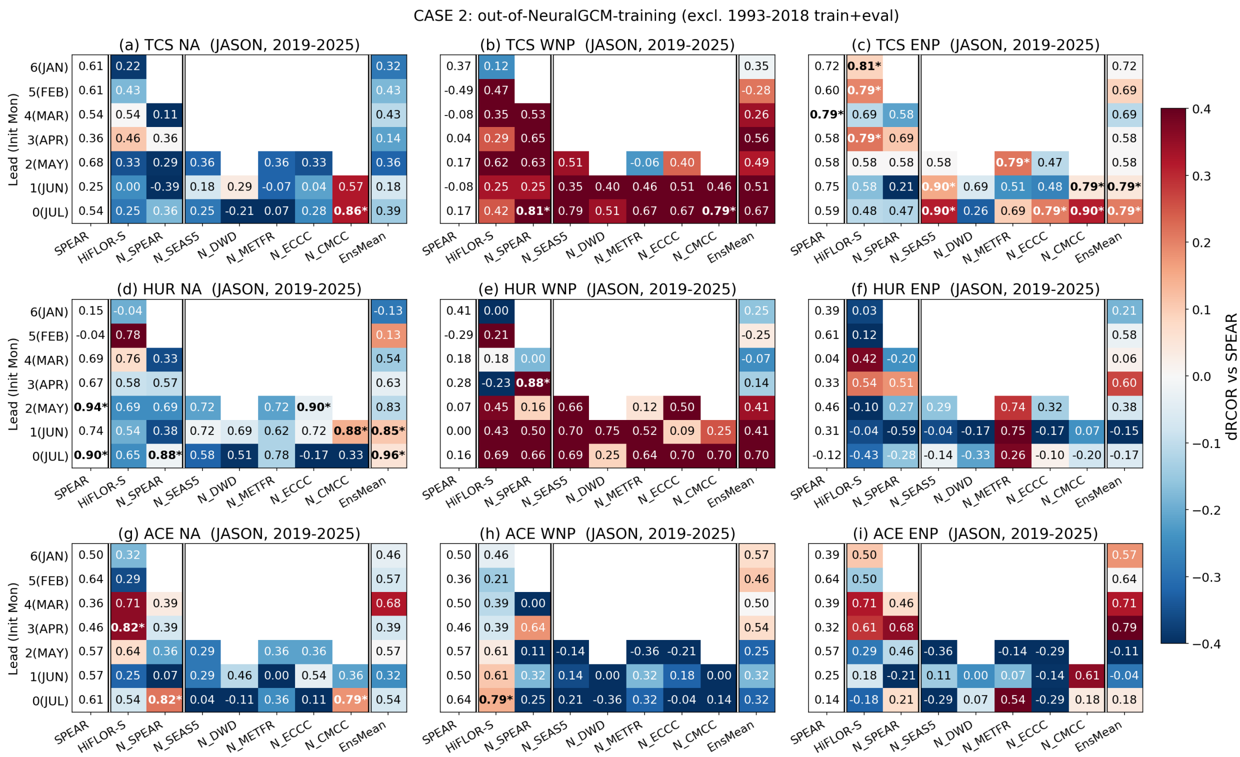

FIG. S8. As in Fig. S7, but for the six NeuralGCM-based configurations. Verification is restricted to the 7 years falling outside both NeuralGCM's own ERA5 training period (1979–2017) and its 2018 verification year (Kochkov et al. 2024): 2019–2025. SPEAR, HiFLOR-S, N_SPEAR, N_SEAS5, N_DWD, N_METFR, N_ECCC, and N_CMCC are shown (ACE2_SPEAR is omitted, as its own training period is not fully excluded by this window); blank cells for the five non-N_SPEAR NeuralGCM configurations at longer leads reflect their shorter (6–7 month) forecast length, as in the main-text figure. Relative to the full-period comparison (Fig. 4), 65% of cells retain the same sign of ΔRCOR; reversals large enough to plausibly alter a qualitative conclusion (|ΔRCOR| ≥ 0.10 in both periods) occur in 11% of cells, split without strong asymmetry between cells where out-of-sample performance is relatively better and relatively worse (10 vs. 14), arguing against leakage of training data into the verification as an explanation for the NeuralGCM-based configurations' competitiveness with SPEAR. TCS skill in the ENP remains high and significant out of sample for most NeuralGCM-based configurations (RCOR up to 0.90), indicating that signal is comparatively insensitive to the choice of verification period.

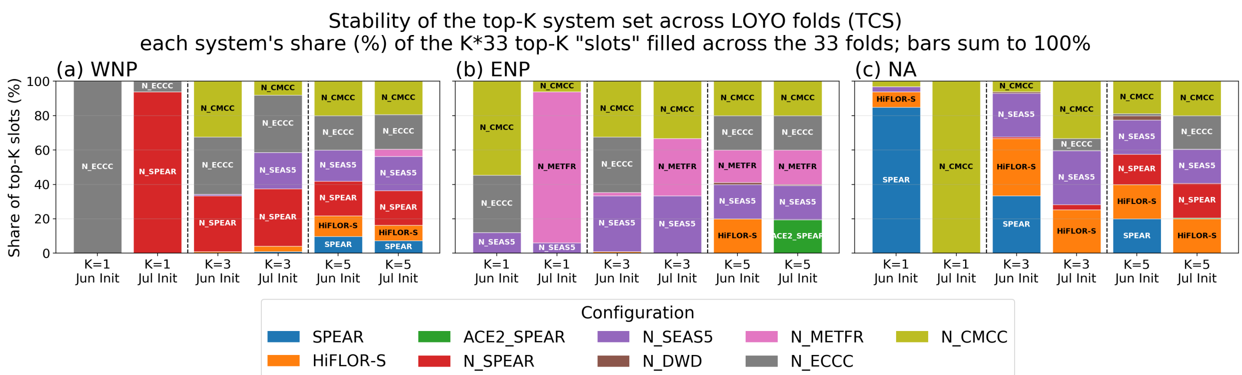

FIG. S9. Each hindcast configuration's share (%) of the $K \times 33$ top-K "slots" filled across the 33 leave-one-year-out folds, ranked by training-fold (32-yr) RCOR against observations, for TCS at (a) WNP, (b) ENP, and (c) NA. Within each panel, groups are K = 1, 3, and 5 (separated by dashed lines), each showing the June and July initializations side by side; segments within a bar sum to 100%. Configuration names are printed directly on segments large enough to hold them; the legend gives the color key for smaller segments.

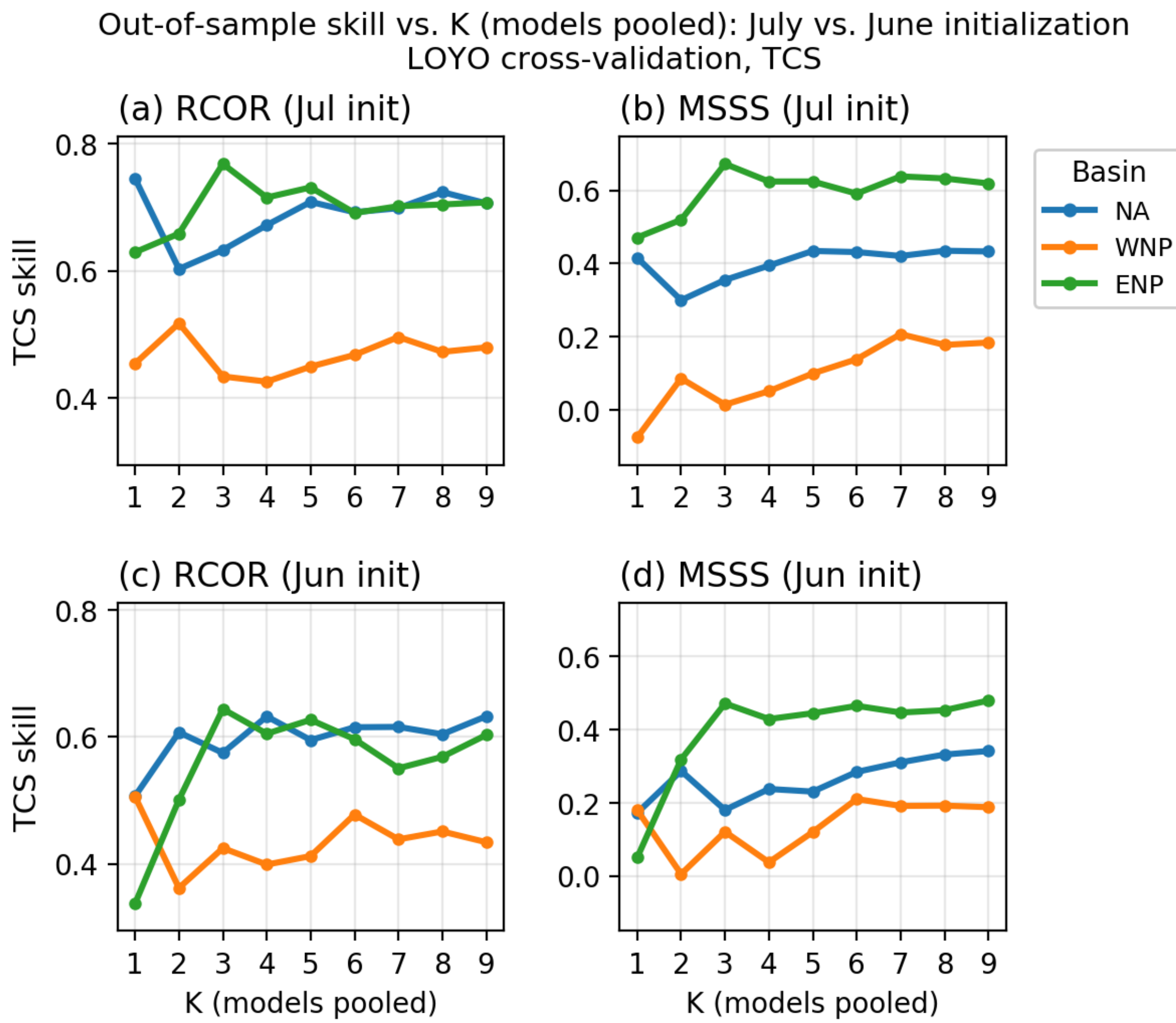

Fig. S10. Out-of-sample RCOR (a, c) and MSSS (b, d) from leave-one-year-out cross-validation, as a function of K (number of top-training-fold-ranked configurations pooled), for TCS at NA, WNP, and ENP: (a, b) July initialization, (c, d) June initialization. For each held-out year, the ratio-calibration factor and the configuration ranking are refit on the other 32 years only, so no information about that year enters either step. $K = 9$ (all nine configurations, equal weight) corresponds to the pooled ensemble in Fig. 3j.

References

Bretherton, C. S., M. Widmann, V. P. Dymnikov, J. M. Wallace, and I. Bladé, 1999: The effective number of spatial degrees of freedom of a time-varying field. *J. Climate*, **12**, 1990–2009, https://doi.org/10.1175/1520-0442(1999)012⟨1990:TENOSD⟩2.0.CO;2.

Kochkov, D., and Coauthors, 2024: Neural general circulation models for weather and climate. *Nature*, **632**, 1060–1066, https://doi.org/10.1038/s41586-024-07744-y.

Watt-Meyer, O., and Coauthors, 2025: ACE2: accurately learning subseasonal to decadal atmospheric variability and forced responses. *npj Clim. Atmos. Sci.*, **8**, 205, https://doi.org/10.1038/s41612-025-01090-0.